https://doi.org/10.5194/egusphere-2025-3952
Preprint. Discussion started: 25 September 2025

Lagrangian Particle–Based Simulation of Aerosol-Dependent Vertical Variation of Cloud Microphysics in a Laboratory Convection Cloud Chamber

Inyeob La[1], Wojciech W. Grabowski[2], Yongjoon Kim[3], Sanggyeom Kim[4], and Seong Soo Yum[4,1]

[1]Climate and Environmental Research Institute, Korea Institute of Science and Technology, Seoul, Republic of Korea
[2]MMM Laboratory, NSF National Center for Atmospheric Research, Boulder, CO, USA
[3]Glocal M&S Co., Ltd., Seoul, South Korea
[4]Department of Atmospheric Sciences, Yonsei University, Seoul, Republic of Korea

Correspondence to: Inyeob La (iyna481@kist.re.kr) and Seong Soo Yum (ssyum@yonsei.ac.kr)

Abstract. We investigate the vertical variability of cloud microphysics in a turbulent convection cloud chamber through large-eddy simulations coupled with a Lagrangian super-droplet (SD) model. Numerical experiments mimic the convection chamber under construction at the Korea Institute of Science and Technology (KIST), employing realistic aerosol size distributions derived from field measurements (VOCALS campaign and Seoul, South Korea). Simulations show that cloud water mixing ratio generally increases with altitude due to continuous droplet activation and growth during ascent, but this vertical gradient weakens significantly as aerosol concentration increases. Enhanced aerosol loading intensifies competition for water vapor, shortening phase relaxation times and suppressing supersaturation variability, resulting in more vertically uniform cloud water mixing ratio profiles. Lagrangian trajectory analyses reveal that upward motion substantially influences droplet growth and activation under clean conditions, but this influence diminishes sharply in polluted environments where rapid vapor depletion limits supersaturation buildup. Furthermore, droplets experiencing sustained upward motion activate more readily, although this effect is weakened considerably in polluted conditions. In a turbulent convection-chamber setting, we quantify how aerosol loading modulates the vertical distribution of cloud-water mixing ratio using LES model with Lagrangian super-droplet tracking, thereby clarifying the coupled roles of vapor competition and vertical transport. Our results emphasize the critical role of aerosol loading in shaping vertical microphysical structures and highlight the interplay between vapor competition and vertical dynamics. These findings provide important insights for improving cloud parameterizations and understanding aerosol-cloud interactions in both controlled laboratory and atmospheric contexts.

1 Introduction

Clouds are key regulators of Earth's climate, influencing radiative balance, precipitation, and atmospheric dynamics. Aerosols, serving as cloud condensation nuclei (CCN), play a crucial role in cloud formation and significantly impact cloud microphysical and optical properties. Human activities have increased aerosol concentrations globally, altering cloud behavior and radiative effects. Recent observations also suggest that reduced ship emissions, resulting from tightened regulations, have substantially decreased aerosol concentrations over the oceans, leading to decreased cloud reflectivity and accelerated global warming (Hansen et al., 2025). Among climate forcing components, aerosol–cloud interactions represent a major source of uncertainty. The IPCC AR6 assigns high confidence to effective radiative forcing from direct aerosol–radiation interactions, but confidence remains low to medium for aerosol–cloud interactions, reflecting continued uncertainties in cloud adjustment processes (IPCC, 2021). This reflects the complex and nonlinear sensitivity of cloud processes to aerosol properties such as size, number, and composition (Seinfeld et al., 2016; Carslaw et al., 2013). Capturing these interactions in models requires detailed understanding of microphysical processes, which are often difficult to constrain from observations. Laboratory cloud chambers have been widely used to probe cloud microphysics under controlled conditions; however, these experiments and measurements are often limited by spatial and temporal resolution, and isolating individual parameter effects remains challenging.

The importance of turbulence-induced supersaturation fluctuations for droplet growth has been highlighted in experimental studies using the Michigan Tech convection cloud chamber (known as the Pi Chamber), where aerosol injection rates are precisely controlled (Chandrakar et al., 2016). These experiments have demonstrated how turbulence broadens cloud-droplet size distributions, particularly at lower aerosol concentrations, which enhances droplet size dispersion and promotes conditions favorable for precipitation formation. Meanwhile, high-resolution numerical simulations that replicate chamber conditions can offer a valuable tool to isolate specific processes—such as droplet activation and supersaturation dynamics—and to explore their sensitivities under well-controlled scenarios. In this context, high-resolution numerical modeling offers a powerful complementary approach. By replicating chamber conditions within a computational framework, models can resolve detailed processes such as aerosol activation, droplet growth, and supersaturation dynamics at scales inaccessible to direct measurement (Grabowski et al., 2024; Thomas et al., 2023). Furthermore, they enable systematic variation of aerosol and thermodynamic properties, facilitating deeper investigation into vertical microphysical evolution and sensitivities to aerosol concentration. This modeling approach is especially valuable for interpreting chamber experiments and extending their implications to atmospheric conditions beyond the laboratory setting (Grabowski & Pawlowska, 2025).

Previous modeling-based laboratory chamber studies (e.g., Thomas et al., 2019; Prabhakaran et al., 2022; Yang et al., 2023) have significantly advanced our understanding of aerosol–cloud interactions; however, most have relied on simplified aerosol representations or bin microphysical schemes. More recent modeling efforts, such as Grabowski et al. (2024), have incorporated realistic aerosol size distributions using the Lagrangian framework. Yet, their focus has largely remained on spatially averaged properties and activation statistics. In contrast, our study centers on the vertical evolution of microphysical structure, using trajectory-resolved analysis to connect individual droplet growth histories with ascent time and S fluctuations, an approach still rare in chamber-scale simulations.

We perform large-eddy simulations (LES) of turbulent moist convection in a laboratory-scale cloud chamber using a Lagrangian particle-based microphysics model. This approach builds upon recent advances in Lagrangian particle-based microphysics (e.g., Shima et al., 2009; Arabas and Shima, 2013; Arabas et al., 2015; Grabowski et al., 2019; Dziekan et al., 2021; Hoffmann and Feingold, 2021; Chandrakar et al., 2022; Yang et al., 2023; Morrison et al., 2024), which support detailed droplet-scale simulations of cloud microphysics, including aspects of aerosol activation and growth dynamics. Following the design specifications of the chamber under construction at the Korea Institute of Science and Technology (KIST), which is intended to support both expansion and convection experiments, the simulation domain is configured to mimic the convection mode of a 1.5 m × 1.5 m × 2 m cloud chamber. Realistic dry aerosol size distributions are adopted from field measurements during the VOCALS campaign (Grabowski et al., 2011) and at a site in Seoul, South Korea (Park et al., 2023a,b), spanning aerosol concentrations from clean to polluted conditions. Through full Lagrangian tracking of individual super-droplets, we quantify how cloud liquid water mixing ratio (q_c) evolves with altitude. We also assess how this vertical structure responds to variations in aerosol concentration, with characteristic timescales of S depletion and droplet ascent. Yang et al. (2023) observed an increasing trend of cloud water mixing ratio with altitude in LES simulations of Pi Chamber. Similarly, Wang et al. (2024) showed that the cloud water mixing ratio maximum occurred near the Pi Chamber top under the lowest aerosol injection rate condition. However, neither study systematically investigated the mechanisms driving this vertical structure. Additionally, Thomas et al. (2022) reported vertical profiles of cloud water mixing ratio from LES simulations of the Pi Chamber, showing a similar trend where cloud water mixing ratio increased with altitude under lower aerosol injection rates, resulting in a mid-level maximum in cloud water mixing ratio. However, this vertical gradient diminished as aerosol injection rates increased. Notably, in Wang et al. (2024), the altitude of maximum cloud water mixing ratio shifted downward—or became less distinct—under higher aerosol injection rates. This trend suggests a potential modulation of vertical condensate structure by aerosol concentration, which our study addresses using Lagrangian trajectory-based microphysical diagnostics across systematically varied aerosol scenarios.

By linking detailed droplet-scale microphysical trajectories to bulk cloud properties under systematically varied aerosol conditions, our findings provide novel insights into the intricate interplay between aerosol properties and cloud microphysical structure. These insights are expected to significantly enhance our ability to accurately represent aerosol-cloud interactions within atmospheric and climate models, ultimately reducing uncertainties associated with cloud feedback mechanisms in climate projections.

2 Model setup

Numerical simulations in this study were performed using the babyEULAG model, a simplified three-dimensional, nonhydrostatic anelastic Eulerian–semi-Lagrangian model coupled with Lagrangian super-droplet microphysics. The dynamic model is a simplified serial version of the 3D nonhydrostatic anelastic Eulerian–semi-Lagrangian (EULAG) model (http://www.mmm.ucar.edu/eulag/), referred to as babyEULAG (Grabowski, 2020). This Lagrangian particle–based approach to microphysics (i.e., using superdroplets; Shima et al., 2009; Grabowski et al., 2019) enables a detailed representation of droplet size distributions and microphysical processes at the particle level. Subgrid-scale turbulence is implicitly represented through the monotone multidimensional positive-definite advection transport algorithm (MPDATA), eliminating the need for explicit subgrid-scale parameterizations. Detailed model descriptions and numerical schemes are provided in Grabowski (2020) and Grabowski et al. (2024). The computational domain was configured to resemble the convection cloud chamber currently under construction at the Korea Institute of Science and Technology (KIST), which is cylindrical with a diameter of 1.5 m and a height of 2.0 m (～3.53 m^3 in volume). While not exactly identical, the model domain closely approximates these dimensions, consisting of 38 × 38 × 101 grid points with uniform grid spacings of 0.04 m horizontally and 0.02 m vertically. A temperature gradient was imposed with bottom and top boundaries set at 299 K and 280 K, respectively, establishing a 19 K difference to drive turbulent moist convection. Sidewall temperatures were fixed at an intermediate value of 289.5 K. The time step for the simulations was set to 0.025 s.

Following Grabowski et al. (2024), the simulations use the babyEULAG configuration with periodic lateral boundaries and rigid-lid lower and upper boundaries. At the lower and upper boundaries, temperature and water vapor mixing ratio are reset at every time step to prescribed values, and the horizontal velocity components satisfy free-slip. To mimic solid sidewalls within the periodic framework, three-grid-point-wide relaxation zones are inserted along the lateral faces; within each wall zone, all three velocity components are relaxed toward zero and thermodynamic fields are nudged toward the prescribed boundary values using a short relaxation time scale of 0.1 s (Grabowski et al., 2024). In contrast to sidewall treatments used previously to promote near-wall evaporation and particle removal—for example, 95% RH at the sidewalls in Grabowski (2020) and recycling of super-droplets entering wall-adjacent zones in Grabowski et al. (2024)—this study prescribes RH = 100% at all boundaries, including the wall zones. To represent laboratory wall-loss processes more realistically, any super-droplet that approaches within 0.1 × dx (for walls normal to x), 0.1 × dy (for walls normal to y), or 0.1 × dz (for the lower or upper boundary) is removed from the domain. This criterion implicitly includes sedimentation losses, because droplets settling under gravity are likewise removed when they come within 0.1 × dz of the lower boundary. The chamber pressure is held constant at 1000 hPa, consistent with Grabowski et al. (2024).

Two aerosol size distributions, identical to those in Grabowski et al. (2024), were considered: one from aircraft measurements during the VOCALS campaign (southeast Pacific; Grabowski et al., 2011) and another from ground-based observations at Yonsei University, Seoul (Park et al., 2023a, b). The VOCALS distribution was bimodal (Aitken and accumulation modes) with an original number concentration of 198.9 cm^{-3}. Following the approach used in Grabowski et al. (2024), this value was rounded to 200 cm^{-3} for ease of comparison and is hereafter referred to as VOCALS (200, CTRL). The Seoul distribution was unimodal, dominated by ultrafine particles typical of polluted urban environments, with an original number concentration of approximately 11,400 cm^{-3}. To maintain consistency with the VOCALS case, this value was similarly rounded to 10K cm^{-3}, hereafter referred to as 10K, and is labeled as Seoul (10K, CTRL). Both distributions maintained their spectral characteristics while systematically scaling total aerosol concentrations between 60 and 10K cm^{-3}. Distributions were discretized into 30 logarithmically spaced bins, ranging from 0.002 to 0.2 μm (VOCALS) and 0.005 to 0.24 μm (Seoul). Following assumptions from Grabowski et al. (2024), NaCl was assumed for VOCALS aerosols, and $(NH_4)_2SO_4$ for Seoul aerosols. These compositions determined critical radius and critical supersaturation for activation. Size-dependent critical radius and supersaturation values were also obtained from Grabowski et al. (2024). Each super-droplet corresponds to a single bin of the 30-bin aerosol distribution, and the model is initialized with 30 super-droplets per grid volume. Figure 1 shows the aerosol

https://doi.org/10.5194/egusphere-2025-3952
Preprint. Discussion started: 25 September 2025

size distributions of the two representative aerosol concentrations (200 and 10K cm⁻³), illustrating how each distribution maintains its spectral shape while the total number concentration varies.

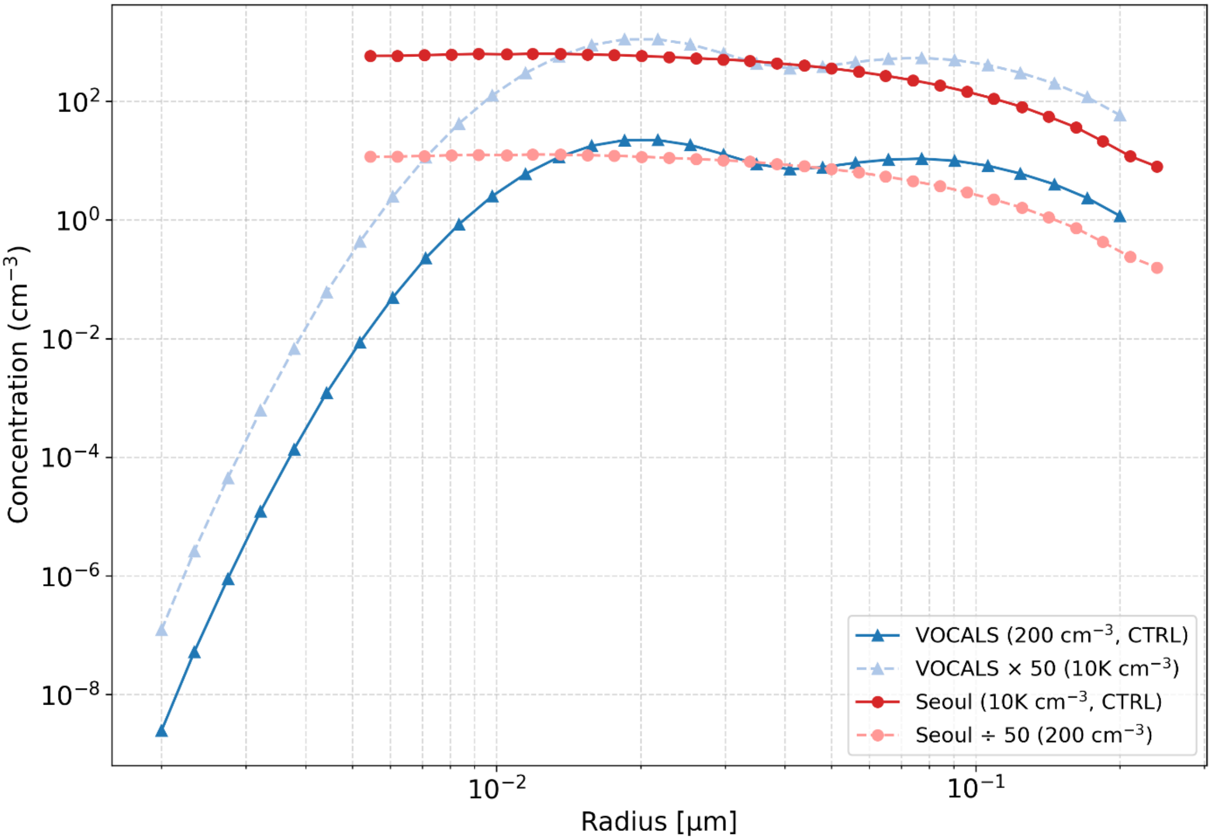

Figure 1. Dry aerosol size distributions used in the simulation experiments, based on measurements during the VOCALS campaign and at a site in Seoul, South Korea. Solid lines show the original observational cases (VOCALS: 200 cm^{-3}; Seoul: 10K cm^{-3}), while dashed or faded lines show size distributions rescaled to match alternative aerosol concentrations (VOCALS × 50 → 10K cm^{-3}; Seoul ÷ 50 → 200 cm^{-3}). Each bin-resolved concentration is used to assign the multiplicity of corresponding super-droplets in the simulation.

To sustain quasi-steady aerosol conditions, aerosol particles were continuously injected at a single grid point near the chamber's top boundary. Compared to the treatment in Grabowski et al. (2024), the present setup offers a more physically realistic representation of both wall-loss and aerosol injection processes. The removal of droplets near boundaries—which implicitly includes droplet sedimentation effects—and sustained aerosol injection reflect laboratory conditions better and support more accurate simulation of quasi-steady aerosol environments. This sedimentation-induced balance was also conceptually highlighted by Prabhakaran et al. (2022). Across all cases, 270 super-droplets (SDs) were injected at each model time step, corresponding to 9 SDs per size bin for the 30-bin aerosol distribution. The physical aerosol injection rate, expressed in terms of particle number concentration per second (cm^{-3} s^{-1}), was controlled solely by adjusting the SD multiplicity. For VOCALS

(200, CTRL), this configuration resulted in 10,800 SDs per second (270 per model time step, 9 SDs per bin), corresponding to approximately 2.3 million physical aerosol particles per second, or 0.51 cm^{-3} s^{-1}. The Seoul (10K, CTRL) case applied a proportionally higher multiplicity to achieve an injection rate of 25.5 cm^{-3} s^{-1}, based on the aerosol size distribution shown in Figure 1. Following Yang et al. (2023), efflorescence was not considered, and all aerosol particles were initialized at their equilibrium haze sizes corresponding to 90% RH, reflecting the expected rapid hygroscopic growth under moist chamber conditions. In contrast, the initial aerosol field at $t = 0$ was initialized with particles at their equilibrium wet sizes corresponding to 100% RH. Figure 2 presents time series of domain-averaged cloud water mixing ratio (q_c), cloud droplet number concentration (N_c), and mean droplet radius (r_m) for both VOCALS (left column) and Seoul (right column) aerosol distributions, sampled at 1-minute intervals. Simulation cases are labeled using the region of origin and aerosol concentration, following the format "VOCALS (200, CTRL)" or "Seoul (10K, CTRL)", where the number indicates the prescribed aerosol concentration (in cm^{-3}) and "CTRL" denotes the baseline case for each distribution. For statistical analysis in this study, cloud droplets (haze particles) are defined as hydrometeors with radii larger (smaller) than 1 μm, following Yang et al. (2023). All three metrics rise rapidly during the first 15 minutes, after which they enter a quasi-equilibrium stage (approximately $t \geq 15$ min). The simulated increase of q_c with aerosol concentration is largely attributable to reduced sedimentation losses under higher droplet number concentrations and smaller mean radius, which reduce terminal velocities and favor condensate accumulation, as conceptualized in Shaw et al. (2023). VOCALS cases exhibit higher N_c and smaller r_m values compared to Seoul cases for the same aerosol concentration, because the VOCALS aerosol size distributions include a greater fraction of larger aerosol particles that activate more readily under similar S conditions. To minimize wall effects, all statistical quantities (e.g., q_c, N_c, r_m) were computed using the data from interior grid points located more than 0.08 m from side walls and 0.1 m from top and bottom walls. Compared to the treatments in Grabowski (2020) and Grabowski et al. (2024), the present setup offers improved realization of simulating both wall-loss and aerosol injection processes. By removing SDs near boundaries (mimicking wall loss) and introducing aerosols via controlled injection, the model more faithfully replicates actual chamber behavior, where particles are lost to walls and replenished through external sources. Indeed, Shaw et al. (2023) observed an increase in q_c with aerosol concentration in their Pi-chamber experiments, consistent with our simulation results. This consistency further underscores that our continuous aerosol injection scheme more accurately captures the physical processes involved, in contrast to Grabowski et al. (2024), who reported no clear increase in q_c with increasing aerosol concentration. These refinements strengthen the physical representativeness of the simulated system.

Droplet collision and coalescence processes were not included in these simulations. This choice is based on Thomas et al. (2022), who demonstrated that collision-coalescence effects are negligible for a chamber height of 2 m, whereas significant impacts emerge only for taller chambers (>4 m). Thus, excluding collision-coalescence allows us to isolate and investigate aerosol-induced effects on condensational growth and droplet activation.

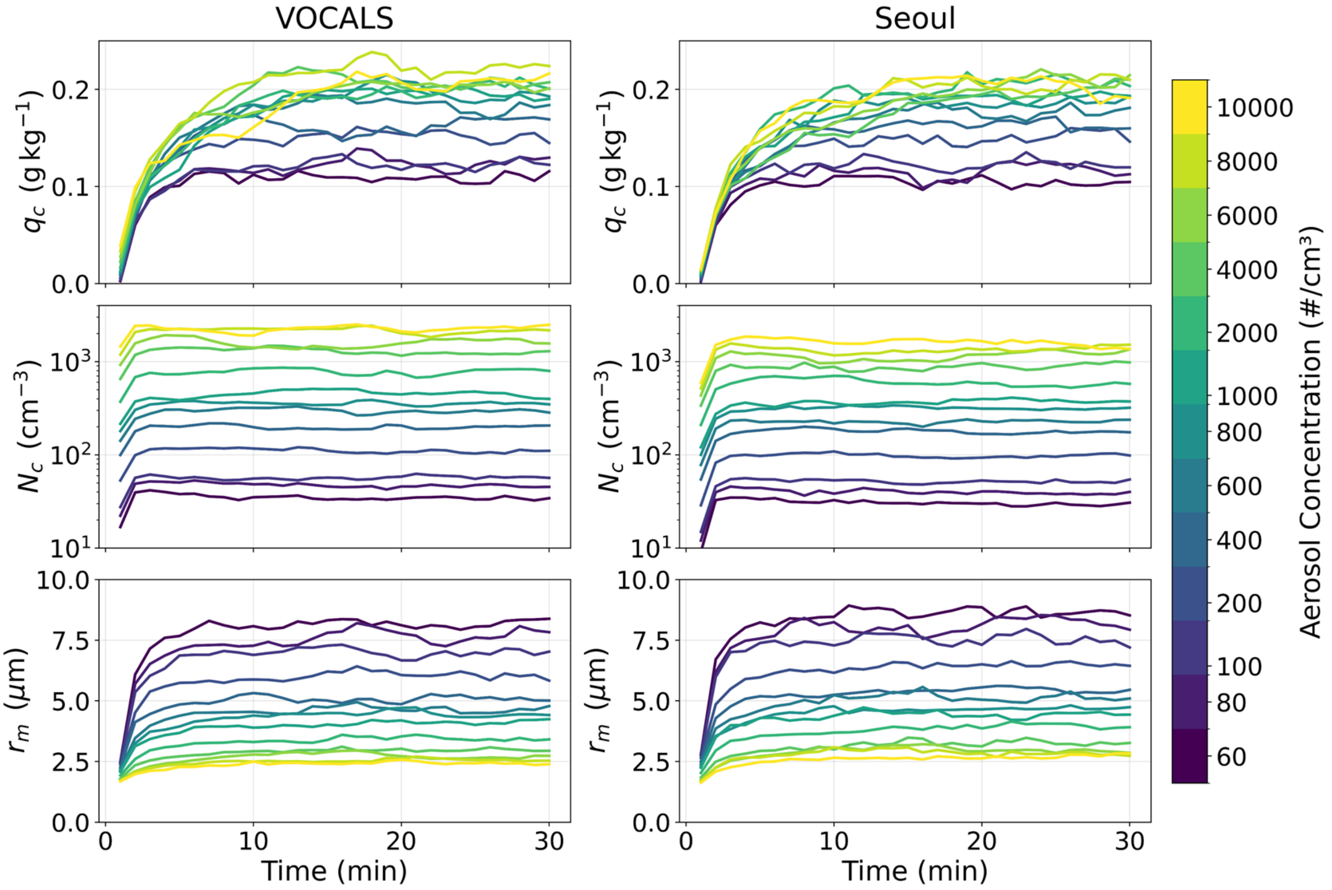

Figure 2. Time series of domain-averaged microphysical variables for VOCALS (left column) and Seoul (right column) aerosol distributions. Each colored line corresponds to a different aerosol concentration (cm⁻³), as indicated in the legends. VOCALS cases range from 60 to 10K cm⁻³ (with 200 cm⁻³ as CTRL), and Seoul cases similarly span 60–10K cm⁻³ (with 10K cm⁻³ as CTRL). Panels from top to bottom show q_c, N_c, and r_m, respectively.

3 Vertical Variability in Cloud Microphysics

3.1 Vertical Structure of Cloud Water Mixing Ratio (q_c)

This section analyzes how q_c varies vertically in the convection cloud chamber. Since simulations reached quasi-equilibrium around 15 minutes, vertical profiles presented are averaged over the subsequent 15 min period (15–30 minutes). Figure 3 (top panels) shows the vertical profiles of domain-averaged q_c for varying aerosol concentrations based on VOCALS and Seoul aerosol distributions. In general, q_c increases with altitude; however, this increase with altitude weakens with increasing aerosol concentrations. At higher aerosol concentrations, the vertical distribution of q_c becomes increasingly uniform, suggesting more spatially homogeneous droplet growth within the cloud chamber. To quantify the vertical variation in q_c, a diagnostic metric,

https://doi.org/10.5194/egusphere-2025-3952
Preprint. Discussion started: 25 September 2025

Δq_c, was introduced. Δq_c indicates the relative difference in q_c between the upper and lower portions of the cloud chamber, capturing the degree of vertical inhomogeneity:

$$\Delta q_c = \frac{\overline{q_c}^{z=1.7\,\mathrm{m}} - \overline{q_c}^{z=0.3\,\mathrm{m}}}{\overline{q_c}^{z=0.3,1.7\,\mathrm{m}}} \times 100\%, \tag{1}$$

where the numerator is the difference in average q_c between the upper (1.7 m) and lower (0.3 m) levels of the chamber, and the denominator is the mean of q_c at both levels, where active cloud formation occurs during the quasi-equilibrium period. Figure 3 (bottom panel) shows that Δq_c decreases with increasing aerosol concentration for both VOCALS and Seoul aerosol distributions. At low aerosol concentrations (60–200 $\mathrm{cm^{-3}}$), Δq_c typically ranges between approximately 9–15%, suggesting a relatively strong vertical increase in q_c that may be attributed to active droplet activation and condensational growth during ascent. Conversely, under high-aerosol conditions ($\geq$ 1000 $\mathrm{cm^{-3}}$), Δq_c drops below 5%, reaching approximately 2% in certain Seoul cases, indicative of a vertically uniform cloud structure. The weakening vertical gradient in q_c with increasing aerosol concentration implies underlying mechanisms: intensified competition for water vapor and therefore low values of supersaturation (*S*), which are examined further in the following section.

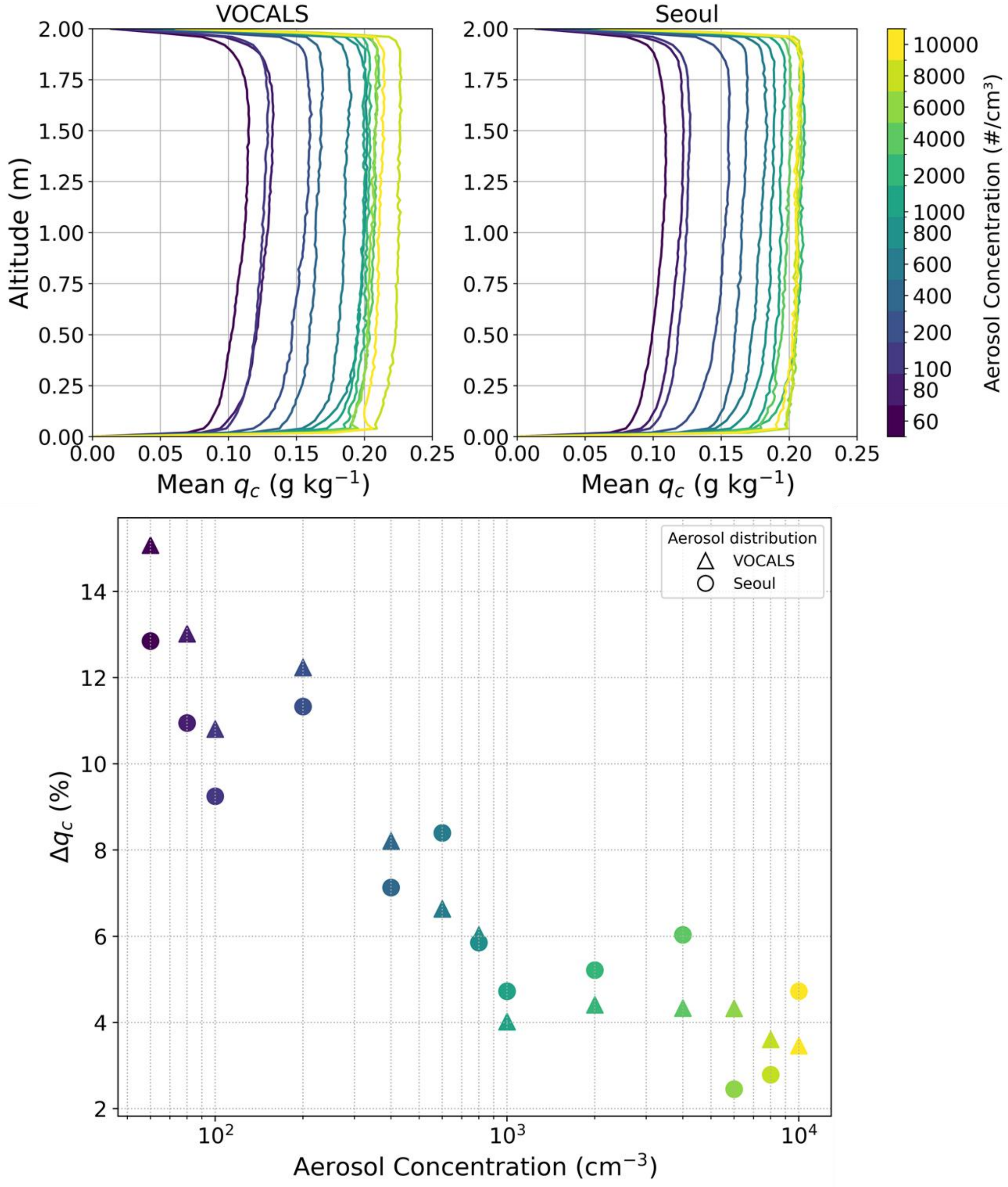

Figure 3. Top panels: Vertical profiles of time-averaged cloud water mixing ratio (q_c) from 0 to 2 m altitude for VOCALS (left) and Seoul (right) aerosol cases at varying aerosol concentrations (60–10K cm^{-3}). Each colored line corresponds to a different aerosol concentration (see legends). Profiles are averaged over the quasi-equilibrium period (15–30 min). Bottom panel: Δq_c as a function of aerosol concentration, where each point represents the averaged value for the quasi-equilibrium period (15–30 min) of each aerosol distribution. Triangles denote VOCALS cases; circles denote Seoul cases.

3.2 Vapor Competition and Supersaturation Dynamics as Constraints on the Vertical Distribution of Cloud Water Mixing Ratio

To elucidate the mechanisms behind the simulated reduction in Δq_c at high aerosol concentrations, relationships between Δq_c and key microphysical parameters were analyzed. Figure 4 shows a strong positive correlation ($R^2 = 0.82$) between Δq_c and the phase relaxation time, which is defined as $\tau_p=(4\pi D_c N_c r_m)^{-1}$, where D_c is a modified molecular diffusion coefficient for water vapor. A longer τ_p, characteristic of low aerosol conditions, is linked to a relatively greater vertical increase in q_c. Physically, τ_p represents the time required for cloud droplets to equilibrate with the surrounding vapor field. When aerosol concentrations are high, the number of droplets increases, leading to stronger competition for available water vapor. As a result, each droplet grows more quickly, consuming vapor rapidly and shortening τ_p. This rapid vapor depletion suppresses the buildup of S during ascent, thereby limiting the vertical increase in q_c. The suppression of vertical S gradients under high aerosol concentrations is clearly illustrated in Figures 5a and 5b, which show vertical profiles of S for the VOCALS and Seoul cases, respectively. As aerosol loading increases, the vertical variation in S becomes gradually reduced, reflecting enhanced competition for water vapor and faster equilibration. In other words, higher N_c leaves insufficient vapor to sustain S during ascent, resulting in vertically almost uniform q_c profiles.

The S histograms in Figures 5c and 5d confirm this narrowing distribution, clearly illustrating the diminished variability and reduced magnitude of S in polluted cases. Figure 6 further demonstrates a systematic decline in the standard deviation of supersaturation (σ_S) with increasing aerosol concentrations, reflecting suppressed S fluctuations in more polluted environments. In addition, the domain-mean supersaturation ($\bar{S}$) also shows a decreasing trend with increasing aerosols (Fig. 6; see symbol colors), indicating an overall reduction in the thermodynamic potential for droplet activation and growth. In our simulations, the largest aerosol mode has a critical S of approximately 0.02%. As aerosol loading increases, $\bar{S}$ steadily falls toward this value, often converging near 0.02% (see Fig. 6). This behavior is consistent with Yang et al. (2025), where $\bar{s}$ approached a single critical value for their monodisperse aerosol. In contrast, because our size distribution spans multiple modes, $\bar{s}$ does not collapse exactly to one number but instead asymptotes to a narrow range just above the largest-mode critical S (～0.02%). As shown in Figure 2, beyond a certain aerosol concentration, domain-mean q_c no longer increases; this stagnation is presumed to result from haze–droplet interactions as described by Yang et al. (2025). Repeated activation–deactivation cycles of small aerosol constrain $\bar{S}$, so increased vapor competition at elevated aerosol concentrations prevents additional droplet activation and growth despite higher aerosol loading. This suppression of S variability parallels the weakening of the vertical q_c gradient discussed earlier. That is, just as vertical differences in q_c become less pronounced with increasing aerosol, so does the vertical structure of s. Figure 2 also shows that each microphysical variable—N_c, r_m, or q_c—exhibits distinct timescales to reach quasi-equilibrium conditions, with these timescales varying systematically with aerosol concentration (see Supplement Figures S1 and S2 for a detailed analysis). Specifically, the increasing aerosol concentration reduces $\bar{S}$ (Fig. 6), influencing these equilibrium timescales.

https://doi.org/10.5194/egusphere-2025-3952
Preprint. Discussion started: 25 September 2025

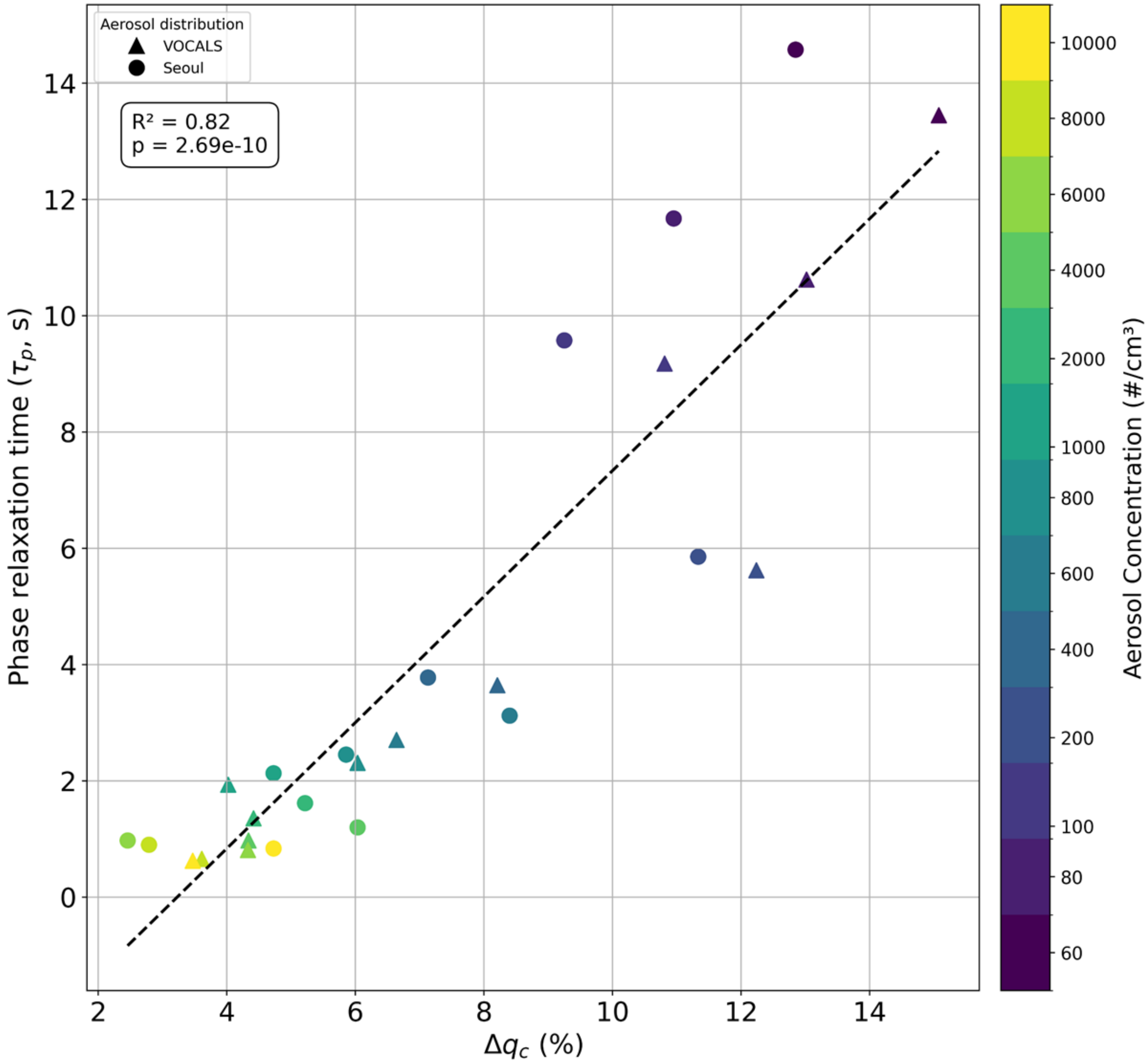

Figure 4. Scatter plot showing the relationship between Δq_c (%) and phase relaxation time (τ_p) for VOCALS (triangles) and Seoul (circles) aerosol cases. Each point represents the averaged value for the quasi-equilibrium period (15–30 minutes).

245

https://doi.org/10.5194/egusphere-2025-3952
Preprint. Discussion started: 25 September 2025

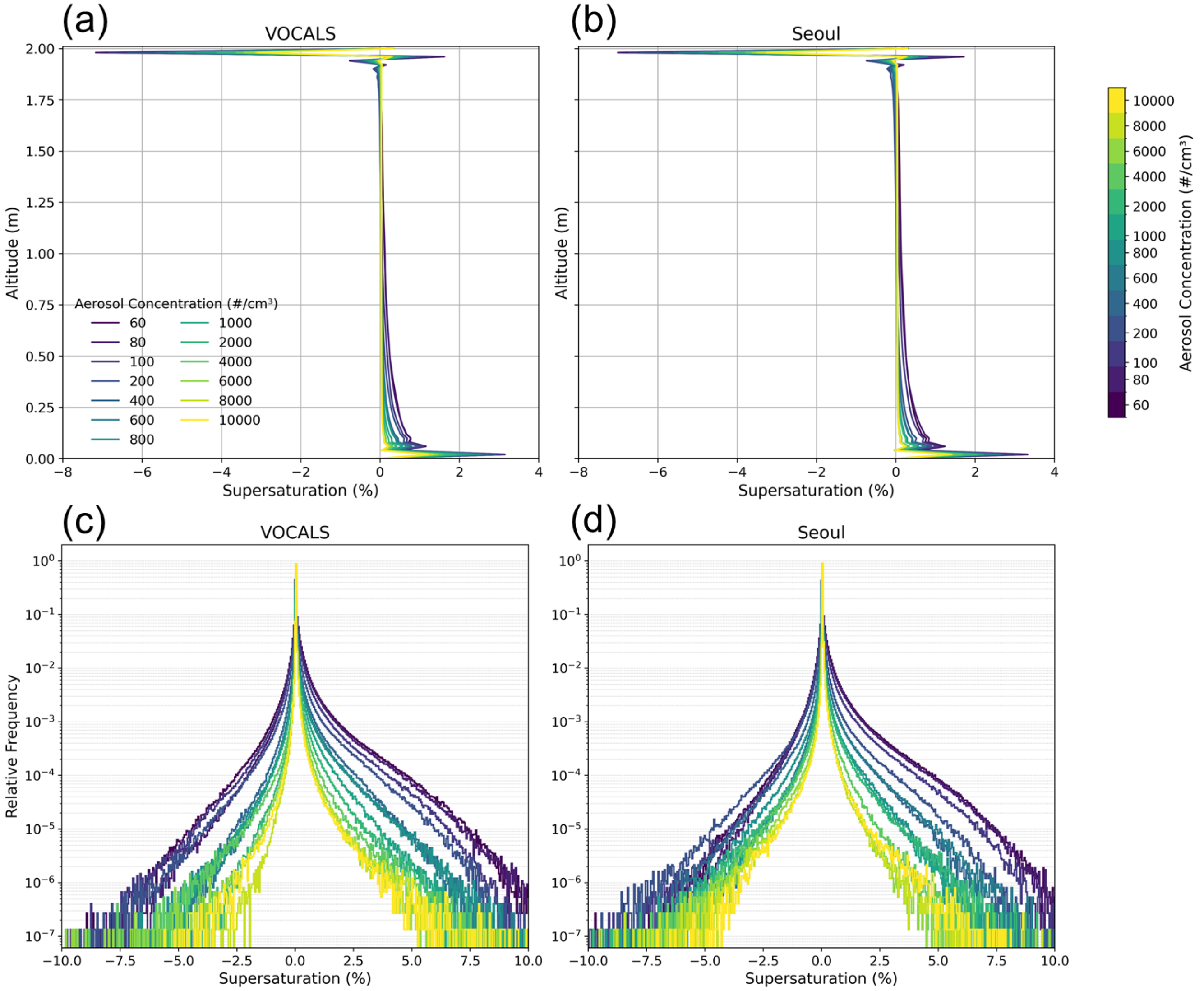

Figure 5. (a, b) Vertical profiles of supersaturation *S* for those same aerosol cases in the VOCALS (a) and Seoul (b) simulations, with line color denoting aerosol concentration. (c, d) *S* histograms for selected aerosol cases in the VOCALS (c) and Seoul (d) simulations.

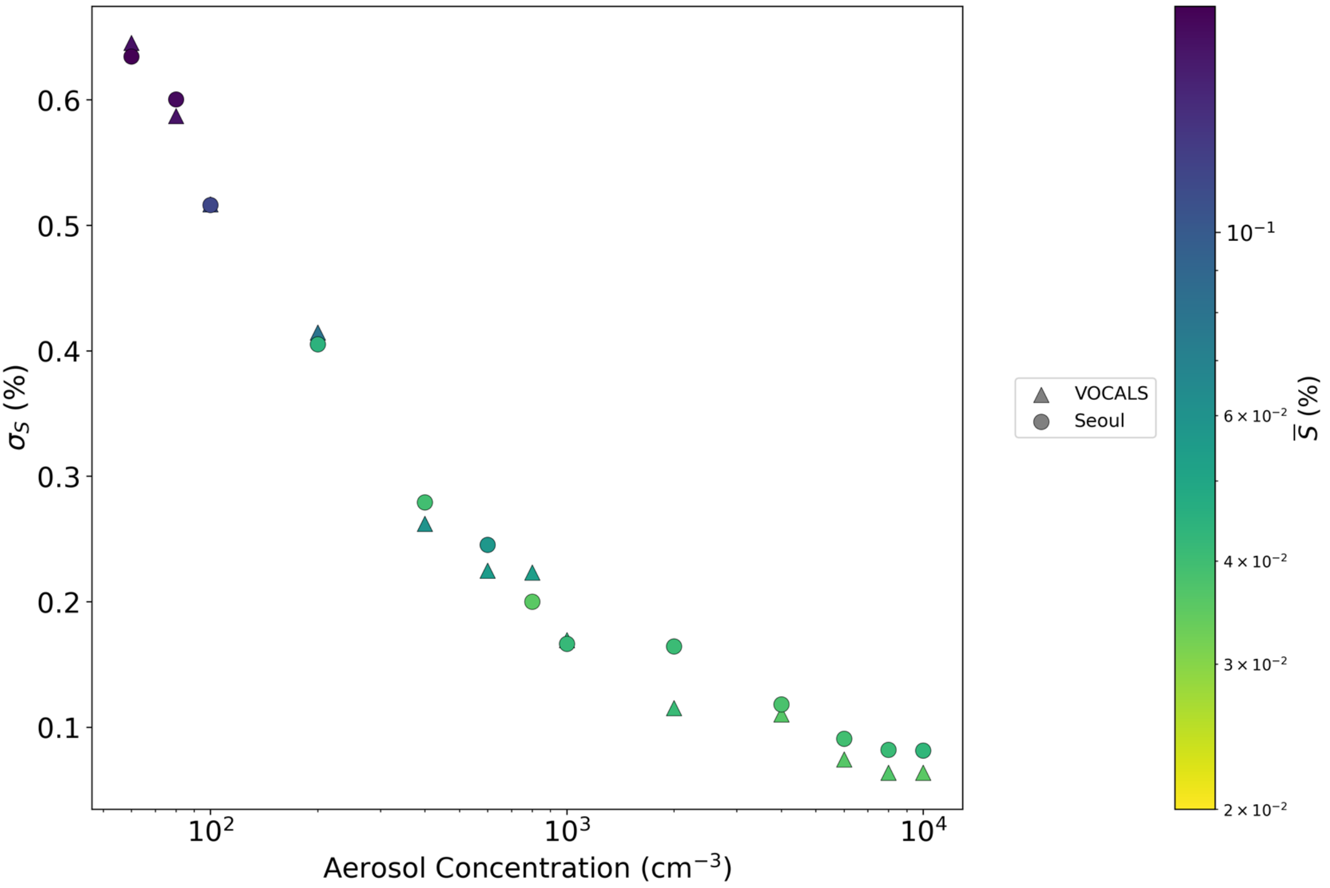

Figure 6. Scatter of supersaturation standard deviation, σ_S, versus aerosol concentration for VOCALS (triangles) and Seoul (circles) aerosol distributions. Marker color denotes the mean supersaturation $\overline{S}$.

To better understand the dynamical origin of this suppressed variability, we examine how *S* interacts with vertical motion. Figure 7 illustrates a significant linear correlation ($R^2 = 0.93$) between σ_S and the correlation coefficient between *S* and vertical velocity (W). This suggests that σ_S is closely tied to the interaction between W and s. In cleaner conditions, the longer phase relaxation time allows *S* to respond more directly to vertical motions, as vapor is not quickly depleted by condensation. However, in polluted conditions, rapid vapor depletion prevents *S* from building up during ascent, thereby reducing its response to W fluctuations. In other words, the rapid vapor consumption reduces *S* response to W variations, effectively decoupling *S* from W. This explains the weakened W–*S* coupling under high aerosol concentrations. As noted by Grabowski et al. (2024), this positive correlation between *S* and W in the chamber arises not from adiabatic cooling driven by the updraft itself, but rather from the mixing of air volumes (parcels) with different thermodynamic properties originating from the lower and upper boundaries. Under constant-pressure conditions, upward motions near the lower boundary transport warmer and moister air there into the chamber, producing positive *S* perturbations. Conversely, downward motions near the upper boundary carry cooler and drier air down into the chamber, generating negative *S* perturbations. Under high aerosol conditions, accelerated vapor consumption reduces droplets' responsiveness to vertical *S* fluctuations, weakening the coupling between *S* and W (small W–*S* correlation) and reducing the variability of *S* (small σ_S). Physical explanation for this is: as aerosol concentration increases, the total droplet surface area also increases, facilitating faster water vapor consumption; Consequently, positive *S* in regions of upward motion is rapidly reduced toward zero; Meanwhile, in regions of downward vertical velocity, the increased droplet surface area accelerates evaporation, supplying water vapor efficiently and thereby driving negative *S* values toward zero fast. Notably, our simulations show clear sensitivity of both positive and negative *S* distributions to aerosol concentration (Fig. S3 in the Supplement), whereas Grabowski et al. (2024) reported negligible sensitivity of negative *S* values to aerosol concentration. This discrepancy is likely attributable to differences in aerosol injection methodologies.

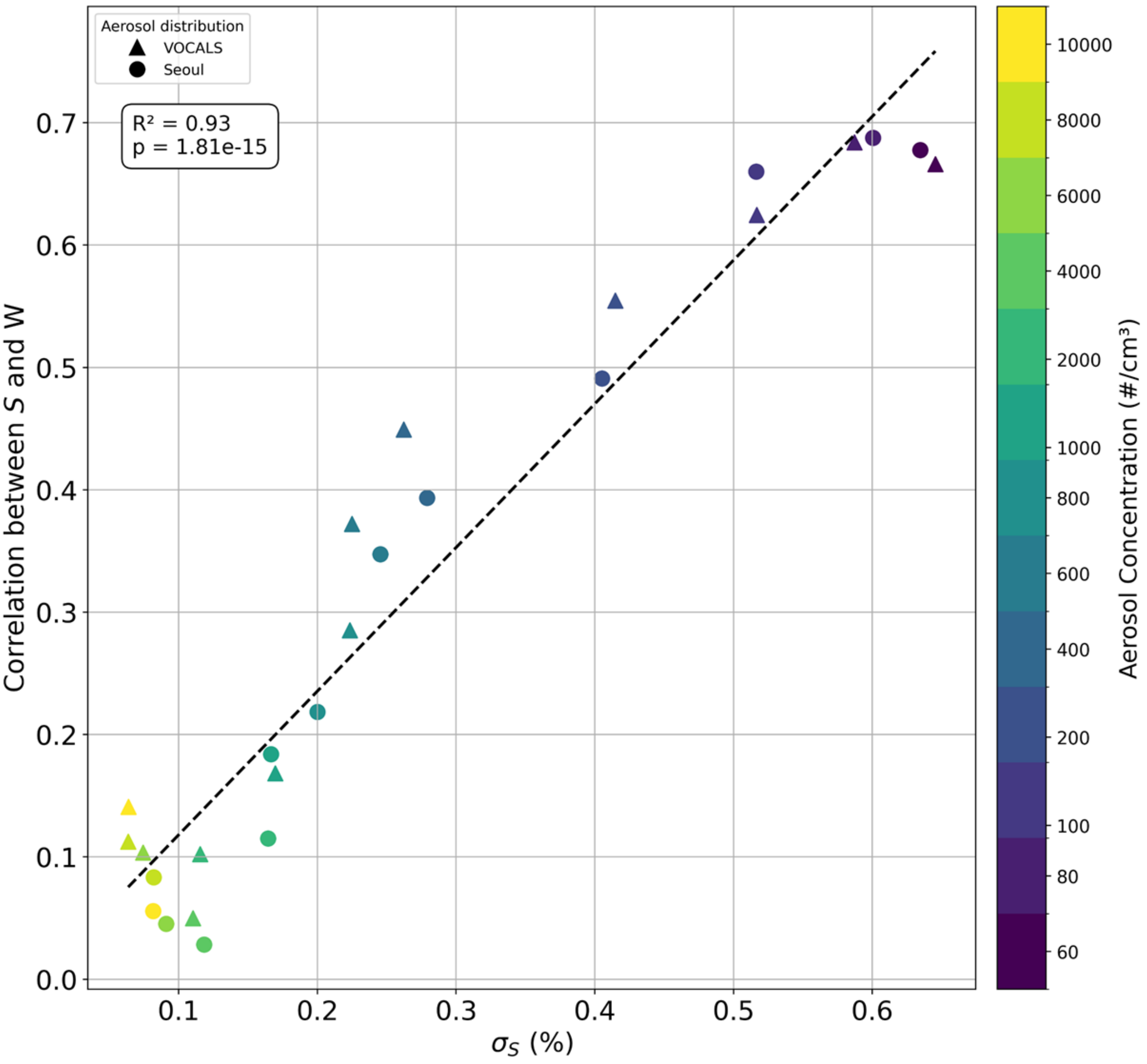

Figure 7. Similar to Figure 4, except showing the relationship between the domain-averaged supersaturation standard deviation (σ_S) and the correlation coefficient between supersaturation (*S*) and vertical velocity (W), computed at the chamber mid-level (z = 1.0 m).

The simulated suppression of vertical gradients in q_c under high aerosol concentrations is most plausibly explained by constraints imposed by τ_p. In polluted environments, the high number of activated droplets dramatically increases the total surface area available for condensation, thereby accelerating vapor depletion and shortening τ_p. This rapid equilibration with the local *S* field causes most condensational growth to occur within the initial stages of ascent. Consequently, droplets complete their growth before experiencing the full extent of vertical *S* variability typically encountered during upward transport. As a result, the effect of vertical motion on condensational growth is diminished, leading to a vertically uniform q_c structure regardless of altitude within the convection chamber. This mechanism highlights how fast microphysical adjustment, rather than turbulent dynamics, primarily governs the vertical distribution of cloud condensate under polluted conditions. To further evaluate this interpretation, the next section presents a Lagrangian analysis that directly compares the characteristic timescales of condensation and turbulent mixing using parcel trajectories, providing a more quantitative framework for understanding the suppression of vertical microphysical variability.

4 Lagrangian Analysis of Droplet Growth and Activation

4.1 Trajectory Analysis of Super-Droplets

To investigate how SDs near the chamber base are vertically transported and dispersed, we performed Lagrangian tracking of all SDs residing within the lowest 0–0.2 m layer of the chamber at a certain point of time. Rather than analyzing a single case, we repeated this tracking procedure across multiple start times during the quasi-equilibrium period, specifically from 900 s to 1780 s at 20 s intervals, to ensure statistical robustness and account for temporal variability of the flow field. Figures 8 and 9 present representative results for two tracking initiation times: 900 s and 1600 s, respectively. Panel (a) in each figure shows time–altitude histograms of SD counts, revealing how SDs rapidly ascend from near the chamber base toward the upper region, subsequently descending and ascending again, with the total count decreasing due to wall losses. Panel (b) in each figure illustrates the spatial distributions of SDs at the initial moments (t = 900 s for Fig. 8, and 1600 s for Fig. 9), while panel (c) depict their positions 20 s later (t = 920 s and 1620 s, respectively). These figures clearly illustrate that most SDs ascend to heights above 1.5 m within approximately 20 s (panels a), although the detailed spatial distribution and vertical extent differ depending on the tracking initiation time (panels c).

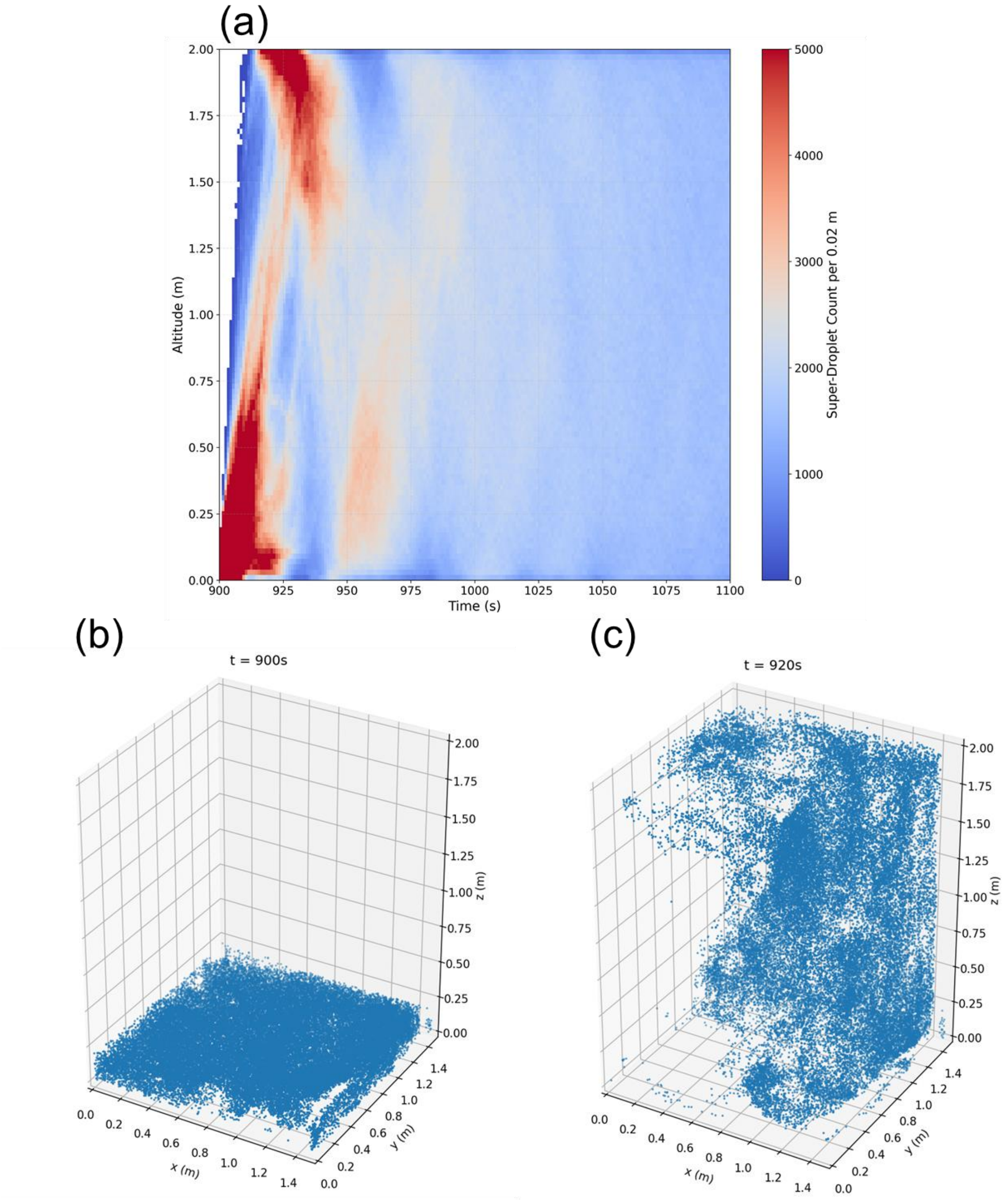

Figure 8. Vertical trajectories of all SDs initiated near the chamber base (z = 0–0.2 m) and tracked forward in time from t=900 s in the VOCALS (200, CTRL) case. (a) Time–altitude histograms showing the temporal evolution of SD vertical positions for the 900 s. (b) 3D spatial distributions of 50,000 randomly selected SDs at the corresponding start times, t = 900 s. Snapshots at t = 920 s showing the same tracked SDs from (b) 20 s after start times.

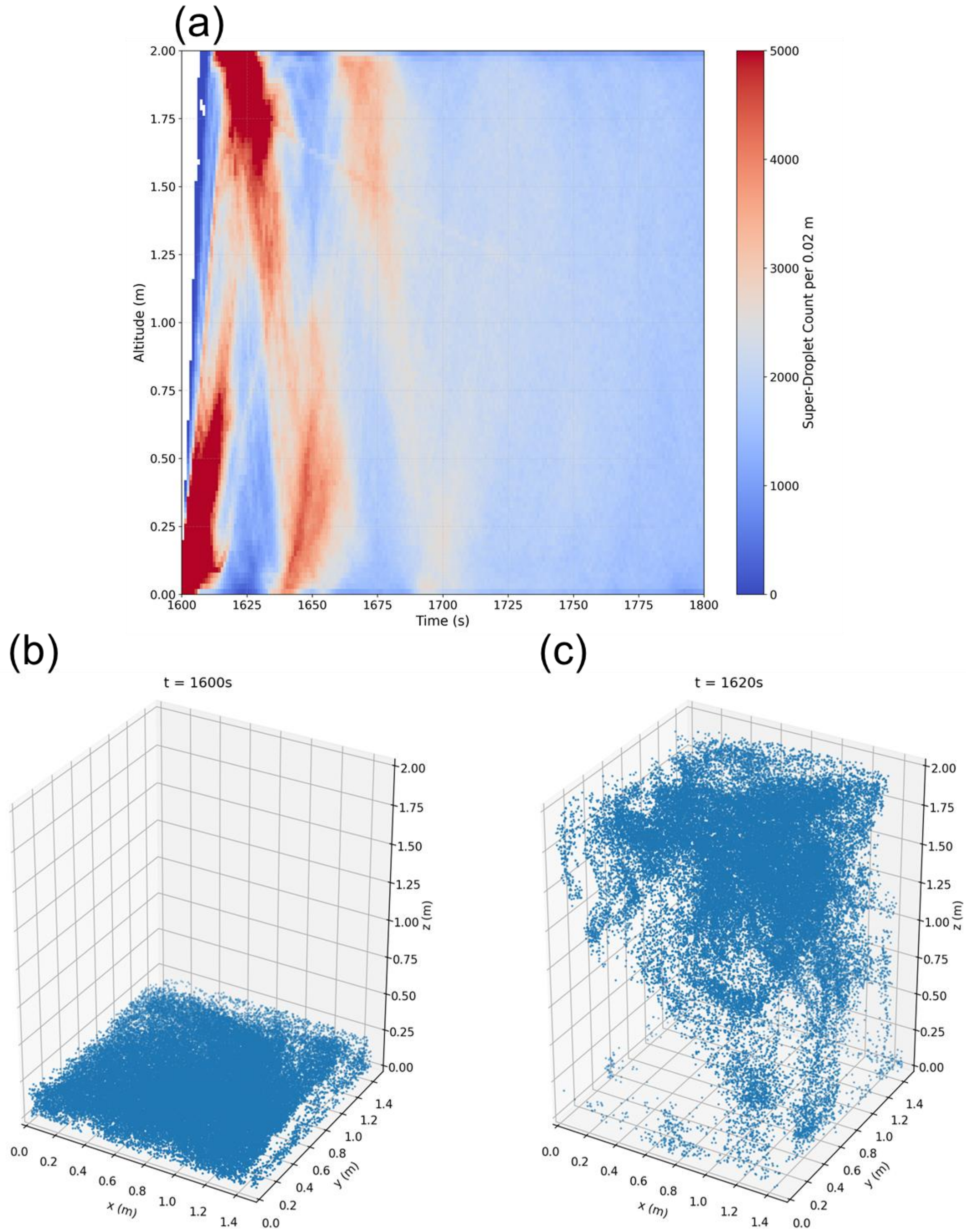

310 **Figure 9. Same as Fig. 8 except for 1600 s start times.**

Given that most SDs ascend from the chamber base to the upper region ($z > 1.5$ m) within approximately 20 s, this ascent time serves as a proxy for the turbulent mixing timescale (τ_m)—the timescale over which S environment evolves. The turbulent mixing timescale can also be independently estimated from the upper height of the chamber (1.5 m) and the turbulent velocity variance ($U \approx 0.06\ \mathrm{m\,s^{-1}}$), derived from the mean turbulent kinetic energy ($\mathrm{TKE} \approx 0.004\ \mathrm{m^2\,s^{-2}}$) as $U = (2/3\ \mathrm{TKE})^{1/2}$. This calculation yields a mixing timescale of approximately 28 s, which is longer than the previously mentioned ascent timescale of ~20 s, likely because the 20 s estimate primarily considers SDs strongly influenced by ascending motion. In contrast, the phase relaxation time (τ_p) becomes significantly shorter under high aerosol concentrations, decreasing from about 14 s in clean cases to around 1 s in polluted conditions (Fig. 4). This disparity can be expressed by the Damköhler number ($\mathrm{Da} = \tau_m/\tau_p$), which quantifies the relative pace of condensation versus turbulent mixing. In polluted environments, $\mathrm{Da} \gg 1$ indicates that condensation occurs much faster than vertical mixing, causing rapid vapor depletion at lower altitudes before S can develop. As a result, condensational growth saturates early in the ascent, suppressing further droplet growth aloft and leading to vertically uniform q_c profiles. This decoupling between vertical motion and S evolution explains the weakened vertical gradients of q_c observed under high aerosol loading. To further investigate how vertical motion influences droplet behavior under these conditions, we analyzed the trajectories of SDs within the lowest 0–0.2 m layer based on their normalized vertical displacement, using the VOCALS (200, CTRL) case as a representative example. Normalized vertical displacement is quantified for each SD over the 20 s tracking interval by comparing its altitude at a certain second to that of the previous second. If the SD ascended, score of +1 was assigned; if it descended, –1; and if there was no change, 0. These 20 values were summed and divided by 20, yielding a normalized score between –1 (entirely descending) and +1 (entirely ascending). Figure 10a shows the evolution over time (0–20 s) of the mean altitude of all SDs grouped by their normalized vertical displacement bins: each line represents the mean altitude of SDs and shaded bands indicate the 25th–75th percentile range. The results demonstrate a clear trend that shows SDs with higher normalized vertical displacement tending to reach significantly higher altitudes. Despite this trend, turbulent motions in the convection chamber allow some SDs with lower normalized vertical displacement to reach relatively elevated altitudes. Figure 10b presents the results averaged over all tracking start times (900 s to 1780 s). For each start time, the mean SD altitude was calculated for each normalized vertical displacement bin, and the shaded bands represent the 25th–75th percentile range of these mean altitude lines across all start times. The overall trend closely resembles that of the single case shown in Figure 10a, confirming the robustness of the normalized vertical displacement metric in capturing vertical transport pathways in the convection chamber.

https://doi.org/10.5194/egusphere-2025-3952
Preprint. Discussion started: 25 September 2025

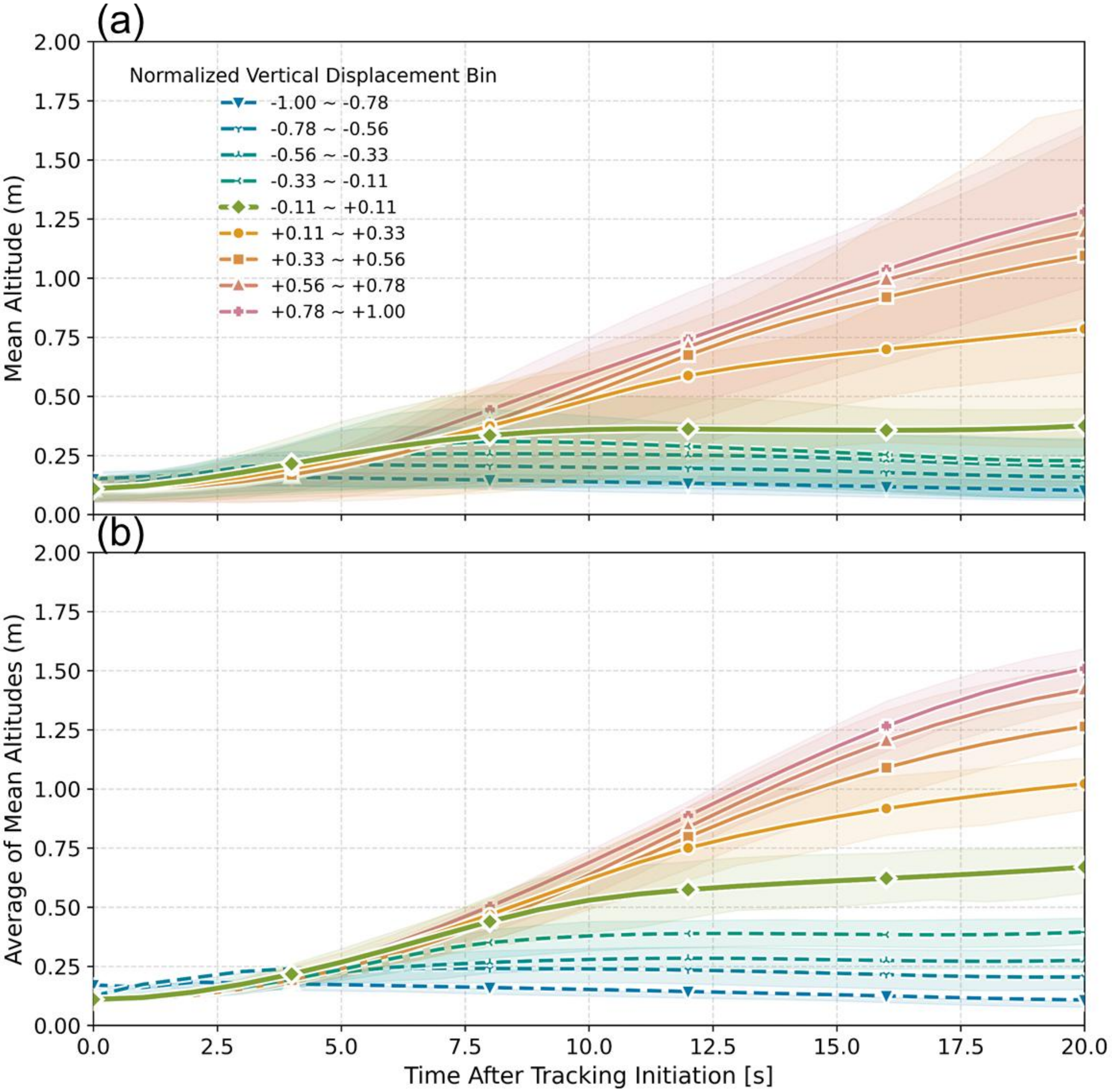

Figure 10. (a) Mean SD altitude as a function of time (0–20 s) after tracking initiation at the single start time of 900 s, computed for each normalized vertical displacement bin in the VOCALS (200, CTRL) case. Shaded bands represent the 25th–75th percentile range of all individual SD trajectories within each bin. (b) Average of mean SD altitudes of all start times (900, 920, …, 1780 s) for the same case. Shaded bands represent the 25th–75th percentile range of the mean altitude lines across all start times. Line colors indicate normalized vertical displacement bins. 345

Building on the Lagrangian tracking framework introduced above, we further investigate how vertical motion influences droplet growth under varying aerosol conditions. Specifically, we analyze the size evolution of individual SDs over 20 s as a function of their normalized vertical displacement. Again, this analysis focuses on SDs initially located near the chamber base (0-0.2 m layer) and tracked upward through turbulent mixing. Tracking was initiated at multiple start times during the quasi-equilibrium period (from t = 900 to 1780 s, every 20 s), and the results were averaged across these intervals. Figure 11a presents the mean normalized droplet growth (dr) of each SD as a function of its normalized vertical displacement. The droplet growth is calculated using:

$$\mathrm{dr} = \frac{\mathrm{r_{end}} - \mathrm{r_{start}}}{(\mathrm{r_{end}} + \mathrm{r_{start}})\,/\,2}, \tag{2}$$

where $\mathrm{r_{start}}$ and $\mathrm{r_{end}}$ are the radius of each SD at the beginning and end of the 20 s interval, respectively. It is clear that SDs with higher normalized vertical displacement generally exhibit larger dr compared to those in the lowest normalized vertical displacement bin (–1.0 to –0.78), particularly for normalized vertical displacement bins up to approximately –0.56 to –0.33, across most aerosol concentrations. This confirms that sustained upward motion enhances droplet growth by exposing SDs to regions of higher s, typically associated with positive W (see Fig. 7). Under such conditions, ascending SDs experience more favorable thermodynamic environments for condensational growth. However, as aerosol concentration increases, dr for ascending SDs becomes less pronounced. In particular, the VOCALS (10K) and Seoul (10K, CTRL) cases show significantly reduced differences in growth between ascending and descending SDs, suggesting that condensational growth becomes increasingly decoupled from vertical motion due to limited S variability under polluted conditions. Figure 11b presents the mean count of SDs in each normalized vertical displacement bin. SDs that were removed due to wall-loss were excluded from the count. Notably, the total SD count tends to increase with aerosol number concentration. This is because higher aerosol loading generally leads to smaller activated droplets with lower fall velocities, thereby reducing sedimentation-driven wall losses and allowing more SDs to remain within the domain throughout the tracking period.

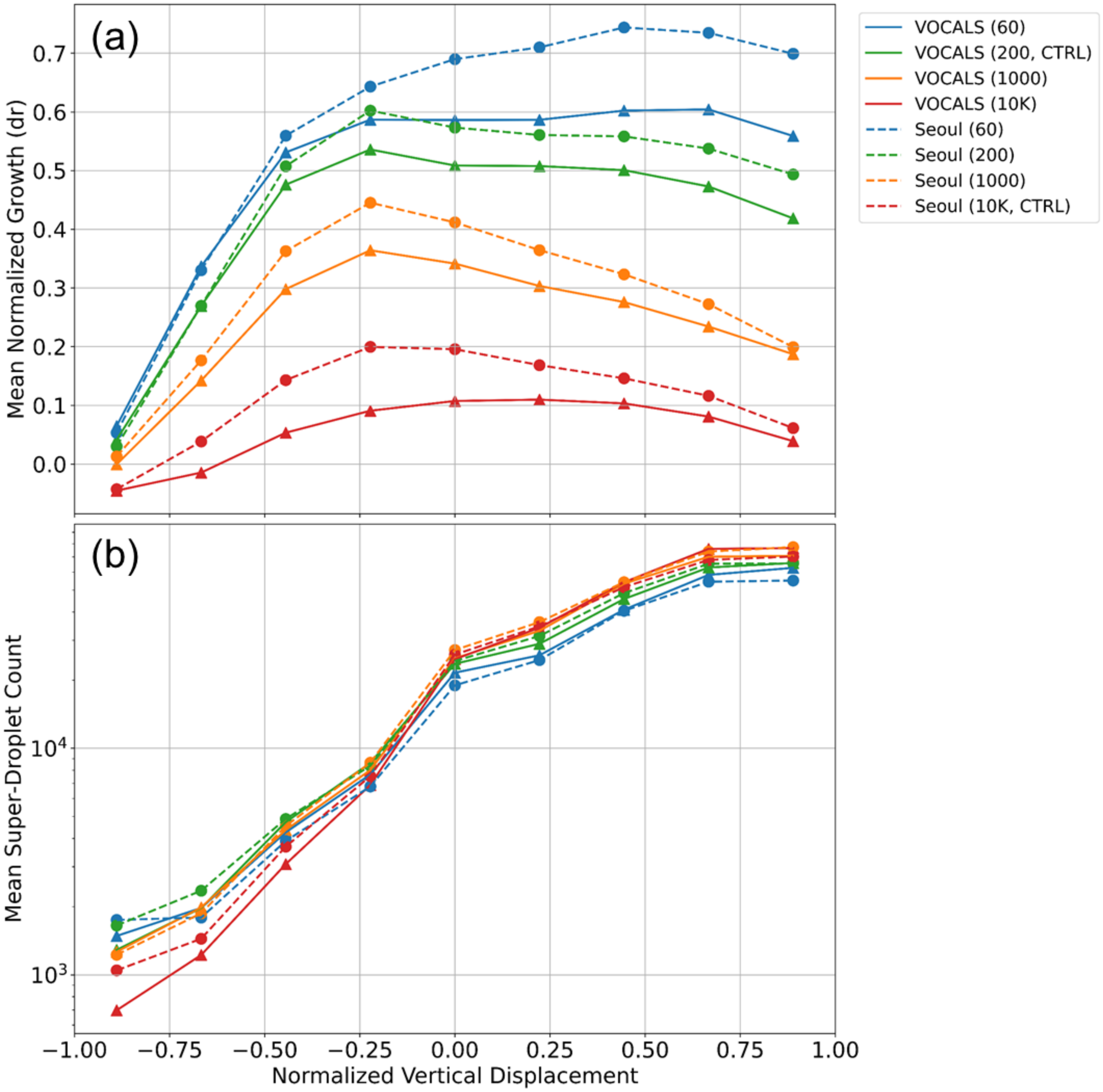

370

Figure 11. Relationship between droplet growth and vertical motion behavior over a 20 s period for SDs initially located within 0–0.2 m of the chamber base at each start time. The analysis is averaged over multiple start times (900–1780 s, every 20 s) during the quasi-equilibrium period. (a) Mean dr as a function of normalized vertical displacement, which quantifies the fraction of time each SD spent ascending. (b) SD count within each normalized vertical displacement bin.

375

A particularly notable feature in Figure 11a is that the maximum dr does not occur at the highest normalized vertical displacement bin but instead peaks near –0.25, for polluted conditions. This counterintuitive result can be explained by the vertical structure of the *S* field within the chamber. As shown in Figures 5a and 5b, *S* is high near the bottom boundary, where warm and moist air perturbations are introduced via wall forcing. Consequently, *S* is spatially confined to the lower region of the chamber and becomes progressively depleted with altitude. SDs with moderate normalized vertical displacement (around –0.25) tend to remain within this lower region ($z \lesssim 0.5$ m; see Fig. 10) and are repeatedly exposed to grid cells containing higher s. In contrast, SDs with higher normalized vertical displacement ascend more rapidly and move beyond the s-generating layer, entering *S*-depleted regions where further growth is limited. This mechanism explains the turnover in dr (except VOCALS (60) and Seoul (60)) in Figure 11a: droplets that ascend too quickly exit the favorable growth environment before maximizing condensational growth. This interpretation is further supported by the normalized vertical displacement-binned mean *S* values shown in Figure 12a, which represent the average *S* encountered by SDs along their trajectories. In all cases, *S* reaches its maximum at a normalized vertical displacement near –0.25 and steadily declines at higher bins. This trend reflects the spatial confinement of *S* production zone near the chamber base and the lack of its regeneration at higher altitudes. Under clean conditions, where vapor competition is weak and the *S* field persists longer due to slower depletion, dr continues to increase with normalized vertical displacement. In contrast, under polluted conditions, rapid vapor consumption depletes *S* more efficiently near the base, limiting droplet growth even for strongly ascending SDs. Figure 12b confirms the positive correlation between normalized vertical displacement and vertical velocity.

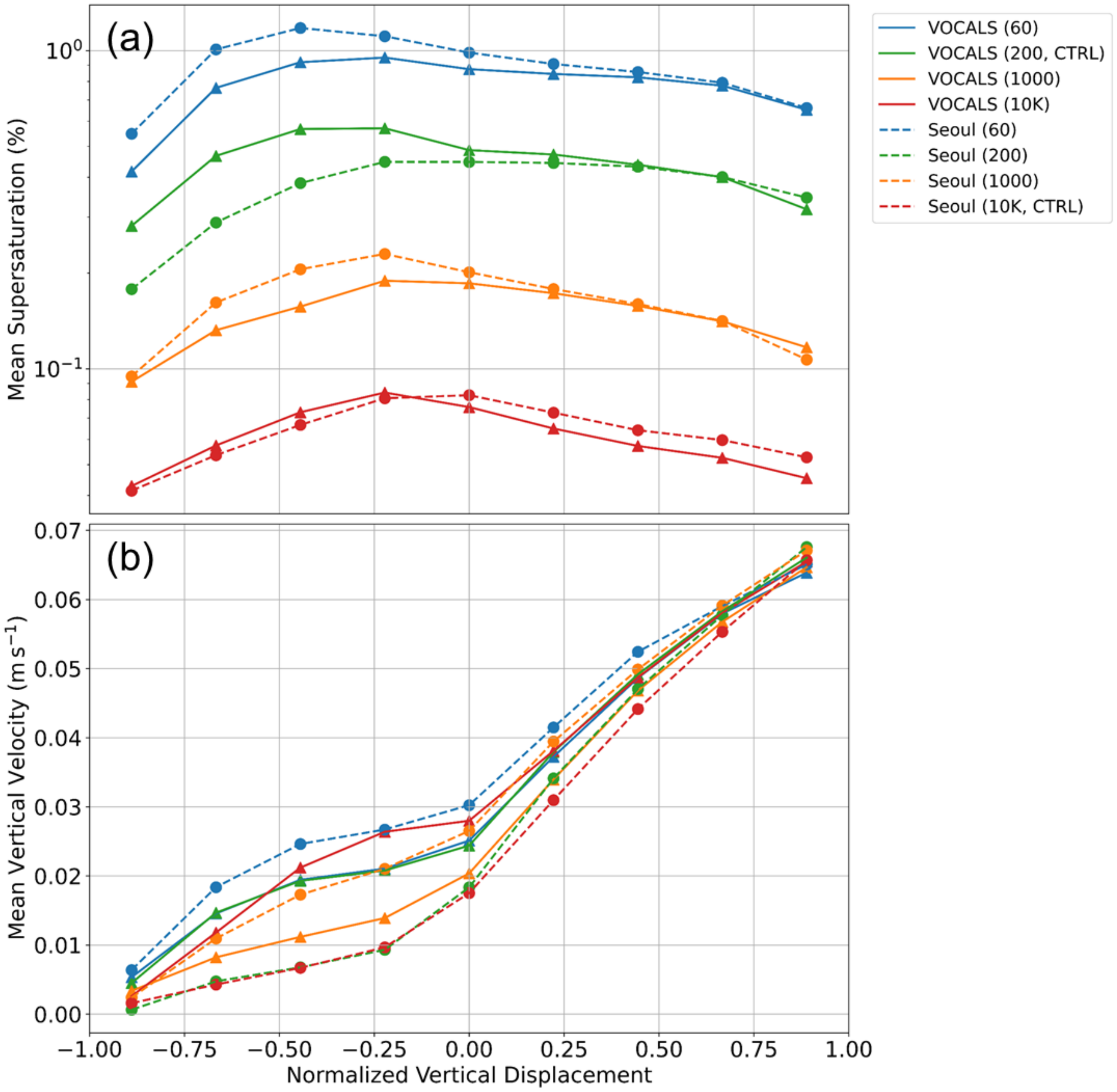

395 **Figure 12. Same as Figure 11, except for (a) mean *S* and (b) mean W.**

https://doi.org/10.5194/egusphere-2025-3952
Preprint. Discussion started: 25 September 2025

4.2 Dependence of Droplet Activation on Vertical Dynamics

To further investigate how vertical dynamics influence cloud microphysical evolution, we analyze the activation behavior of unactivated SDs initially located near the chamber base (z = 0–0.2 m) under varying aerosol conditions. Rather than focusing on a single time, we apply this analysis across multiple start times during the quasi-equilibrium period (900–1780 s, every 20 s). The activation fraction is defined as the ratio of the number concentration of SDs that become activated during the 20 s tracking interval to the total number concentration of initially unactivated SDs located near the chamber base (z = 0–0.2 m). Figure 13a shows the activation fraction of SDs binned by normalized vertical displacement, averaged for all start times. Each SD was tracked for 20 s after its respective start time, and its activation status was evaluated. The activation fraction generally increases with normalized vertical displacement, indicating that upward motion enhances the likelihood of activation by transporting SDs into regions of higher s. The highest activation fraction does not occur at the most strongly ascending bin. In many cases, it peaks around a normalized vertical displacement of approximately –0.25. This pattern closely resembles dr trends discussed earlier (Fig. 11), where SDs with moderate normalized vertical displacement experienced the largest size increase. In both dr (Fig. 11) and the activation fraction (Fig. 13) analyses, the key factor is that SDs with normalized vertical displacement near –0.25 tend to remain longer within the lower chamber layer ($z \lesssim 0.5$ m), where S is enhanced by mixing of air parcels originating from contrasting thermal and moisture conditions at the boundaries. As shown in Figure 5, S values tend to be higher near the bottom boundary and gradually decrease toward zero with increasing distance from the bottom boundary. These SDs are repeatedly exposed to favorable microphysical conditions, increasing their chance of activation and growth. In contrast, SDs with higher normalized vertical displacement ascend more quickly out of this region and enter layers where S has already been depleted, thereby limiting both activation and growth. As aerosol concentration increases, the overall activation fraction declines due to intensified vapor competition. In highly polluted cases such as VOCALS (10K) and Seoul (10K, CTRL), even strongly ascending SDs show limited activation, and the difference between ascending and descending SDs becomes small. This suggests that condensational growth depletes vapor faster than it can be replenished by turbulent mixing, reducing S variability and diminishing the impact of vertical motion. Figure 13b shows the mean number of unactivated SDs near the chamber base that remained within the simulation domain and were fully tracked for 20 s after each start time (t = 900–1780 s, every 20 s), binned by normalized vertical displacement. Figures 14a and 14b illustrate the 3D distribution of unactivated SDs at t = 1600 s (upper panels) and of activated and unactivated SDs t = 1620 s (lower panels), for two representative cases of VOCALS (200, CTRL) and VOCALS (10K). Under clean condition activation is relatively widespread, but under polluted conditions only a small number of SDs activate.

These results collectively suggest that, under high aerosol loading, droplet activation becomes increasingly independent of vertical motion due to limited thermodynamic potential for nucleation. These Lagrangian findings reinforce the τ_m–τ_p perspective. Under polluted conditions, ($Da \gg 1$), intensified vapor competition rapidly depletes available water vapor, leading to early saturation of condensational growth at lower altitudes. This process not only reduces the overall magnitude of droplet growth and activation fraction, as shown in Figures 11 and 13, but also weakens the dependence of these microphysical processes on vertical transport, as quantified by normalized vertical displacement. As a result, the q_c structure becomes increasingly uniform in the vertical. This highlights that the homogenization of cloud condensate in the vertical direction under polluted conditions might be primarily driven by microphysical timescale constraints

In comparing VOCALS and Seoul cases for the same aerosol concentrations, dr is greater for Seoul cases, whereas the activation fraction is higher for VOCALS cases (Figs. 11 and 13). This difference arises because VOCALS aerosols contain more large particles that readily activate, resulting in higher N_c and activation fractions. In contrast, Seoul aerosols include more small particles that activate less efficiently, leading to fewer activated droplets. Consequently, these fewer droplets face reduced competition for water vapor, promoting greater individual growth compared to VOCALS.

https://doi.org/10.5194/egusphere-2025-3952
Preprint. Discussion started: 25 September 2025

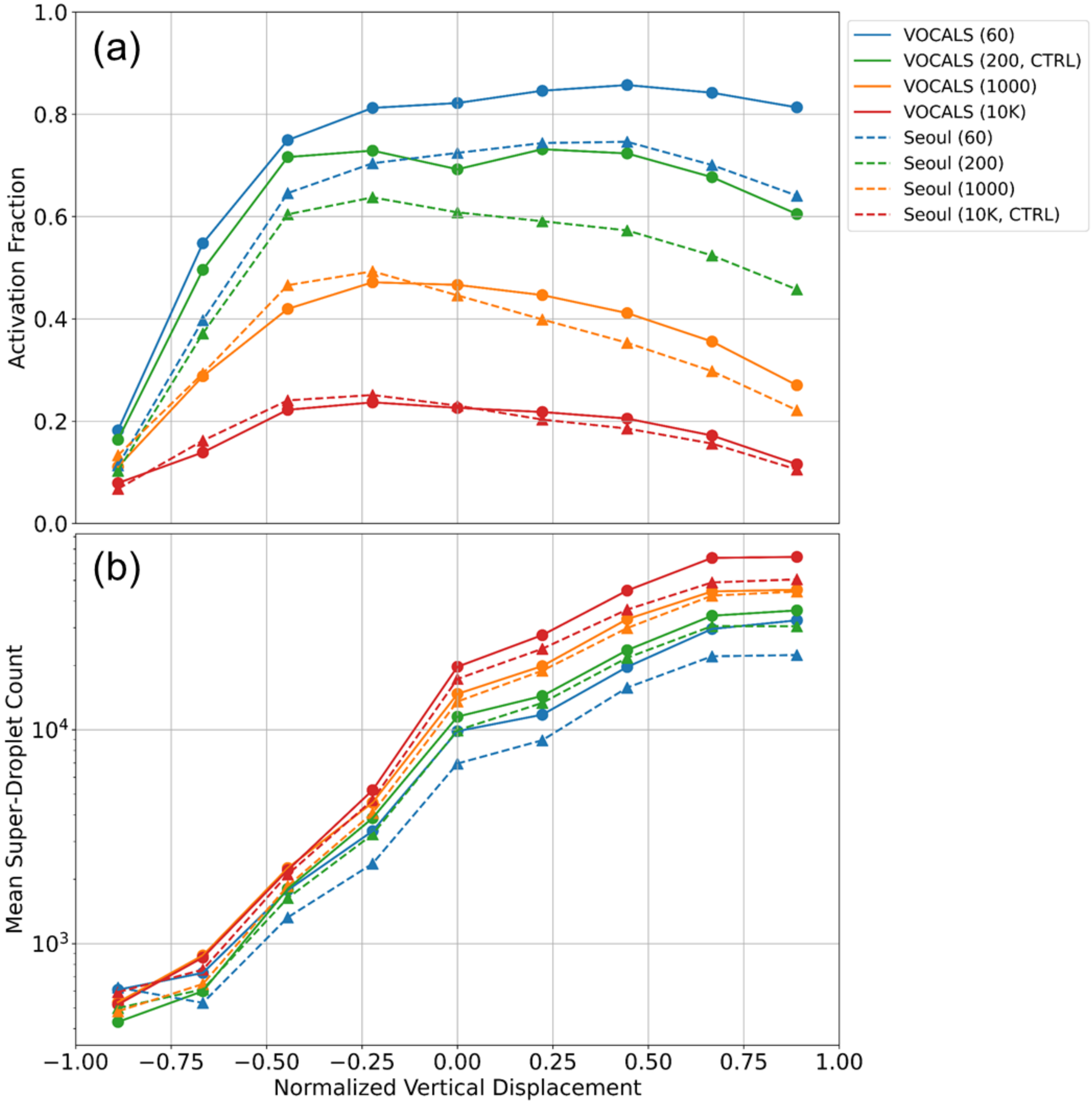

Figure 13. (a) Activated droplet fraction over a 20 s interval, binned by normalized vertical displacement. The fraction is calculated by dividing N_c of SDs that are in the activated state at $t = t_{start} + 20$ s by the N_c of unactivated SDs initially located near the chamber base ($z = 0$–0.2 m) at each start time. The analysis is averaged over multiple start times during the quasi-equilibrium period. (b) Mean count of SDs that were successfully tracked over each 20 s interval (starting from t = 900 s to 1780 s every 20 s), binned by normalized vertical displacement. 440

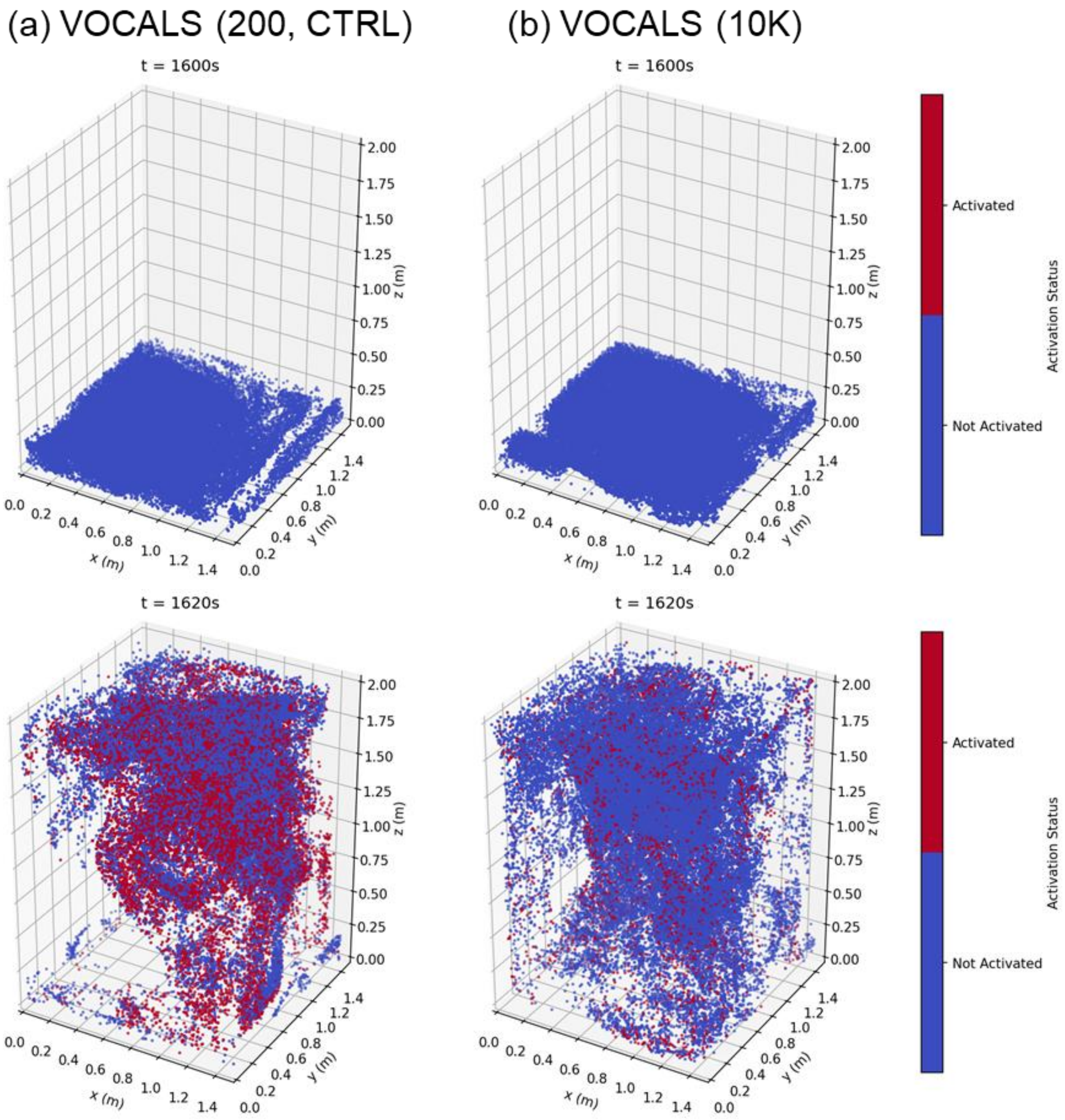

445

Figure 14. 3D spatial snapshots of SDs at t = 1600 s (top) and t = 1620 s (bottom), shown for VOCALS (200, CTRL) (a) and VOCALS (10K) (b). Red points represent SDs that became activated, while blue points remain unactivated. Only 50,000 randomly sampled SDs at t = 1600 s are shown for visualization.

https://doi.org/10.5194/egusphere-2025-3952
Preprint. Discussion started: 25 September 2025

5 Concluding Remarks

This study investigated how varying aerosol concentrations influence cloud microphysical evolution and vertical structure using idealized simulations of a turbulent moist convection cloud chamber. The simulations employed a large-eddy simulation (LES) coupled with a Lagrangian super-droplet method (SDM), configured to represent turbulent convection-mixing processes in a laboratory-scale chamber currently under construction at the Korea Institute of Science and Technology (KIST). Differences emerged in the vertical distribution of cloud water mixing ratio under varying aerosol conditions. At low aerosol concentrations, droplets experienced sustained condensational growth during ascent, producing significant vertical gradients in cloud water mixing ratio due to prolonged exposure to supersaturation (*S*). Conversely, at high aerosol concentrations, rapid vapor depletion at lower altitudes resulted in early saturation of droplet growth, yielding a vertically uniform cloud water mixing ratio profile. The Damköhler number ($\mathrm{Da} = \tau_m/\tau_p$), the ratio of turbulent mixing timescales (τ_m) to microphysical timescales (τ_p), effectively characterized this transition: high aerosol conditions corresponded to large Da ($\gg 1$), indicating that condensation occurred much faster than vertical mixing, leading to decoupling droplet growth from vertical motion. Complementary Lagrangian analyses provided further insights into droplet growth and activation. Under low aerosol conditions, droplet growth (dr) and activation strongly correlated with upward displacement (normalized vertical displacement), reinforcing the critical role of sustained exposure to regions of enhanced *S* near the chamber base. However, at elevated aerosol concentrations, this correlation weakened significantly due to intensified vapor competition, limiting *S* variability. Thus, under polluted conditions, droplet activation became increasingly independent of vertical motion, reinforcing the vertical homogenization of cloud water mixing ratio. These simulation results offer several practical implications for cloud chamber experiments. First, the identified transition in cloud water mixing ratio vertical structure—governed by the relative timescales of condensation and mixing—provides a robust diagnostic framework to interpret experimental observations. Second, specific microphysical signatures, particularly vertical uniformity in cloud water mixing ratio under polluted conditions, serve as clear observational markers to diagnose aerosol effects within controlled laboratory settings. Accordingly, the design and interpretation of future chamber experiments may benefit from considering these mechanisms, as they could fundamentally influence how droplet activation and condensational growth manifest under varying aerosol conditions.

Moreover, this study enhances process-level understanding of cloud microphysics by elucidating how aerosol-induced changes in *S* variability and droplet activation mechanisms directly impact the vertical distribution of cloud condensate. Although the *S* generation mechanism in the chamber differs fundamentally from atmospheric clouds—being driven by the mixing of air parcels originating from both lower and upper boundaries with contrasting thermodynamic properties rather than adiabatic cooling—the interplay between microphysical timescales and turbulent dynamics remains broadly relevant, offering valuable insights into aerosol-cloud interactions. Importantly, this is the first study to identify the mechanisms governing the aerosol-dependent vertical distribution of cloud condensate in a laboratory convection chamber using Lagrangian super-droplet tracking. This novel approach reveals how vertical motion and vapor competition jointly modulate droplet growth, offering a new process-based framework for interpreting chamber experiments and guiding cloud parameterizations.

We acknowledge that *S* profiles in Figure 5a,b exhibit oscillations near the lower and upper boundaries. However, Pi-chamber simulations that calculate boundary fluxes using Monin–Obukhov similarity theory—i.e., parameterizing surface sensible- and latent-heat fluxes and determining boundary conditions for velocities, temperature, and water vapor from the same framework—also report a qualitatively similar increase in cloud water mixing ratio with height (Yang et al., 2023; Thomas et al., 2022; Wang et al., 2024). This convergence across configurations supports our main interpretation: the aerosol-driven weakening of the vertical gradient of q_c—and the emergence of vertically uniform q_c at high aerosol loading—are not artifacts of boundary-condition choice but reflect robust interactions between microphysical and turbulent timescales ($Da \gg 1$). Nevertheless, boundary conditions for laboratory convection chambers are not yet standardized and can influence *S* variability and activation statistics near walls. Further research on boundary-condition and flux formulations is needed, including direct assessment of specified-state versus flux-based plate thermodynamics, and lateral-wall treatments, within a common dynamical–microphysical framework and with validation against measurements to quantify their influence on near-wall *S* and activation.

Data availability The presented data are available from the corresponding author upon request (iyna481@kist.re.kr).

Author contributions IL wrote the original manuscript draft; SSY acquired funding and administered the project; IL and SK conducted the investigation; WWG and YK developed software; SSY supervised the research; IL, WWG, SK, and SSY reviewed and edited the manuscript.

Competing interests The authors declare that they have no conflict of interest.

Acknowledgments. This work was supported by KIST Institutional Grant, 2E33101 and by the Yonsei Signature Research Cluster Program of 2024 (2024-22-0162).

References

Arabas, S., Jaruga, A., Pawlowska, H., and Grabowski, W. W.: Libcloudph++ 1.0: A single-moment bulk, double-moment bulk, and particle-based warm-rain microphysics library in C++, Geosci. Model Dev., 8, 1677–1707, https://doi.org/10.5194/gmd-8-1677-2015, 2015.

Arabas, S. and Shima, S. I.: Large-eddy simulations of trade wind cumuli using particle-based microphysics with monte Carlo coalescence, J. Atmos. Sci., 70, 2768–2777, https://doi.org/10.1175/JAS-D-12-0295.1, 2013.

Carslaw, K. S., Lee, L. A., Reddington, C. L., Pringle, K. J., Rap, A., Forster, P. M., Mann, G. W., Spracklen, D. V., Woodhouse, M. T., Regayre, L. A., and Pierce, J. R.: Large contribution of natural aerosols to uncertainty in indirect forcing, Nature, 503, 67–71, https://doi.org/10.1038/nature12674, 2013.

Chandrakar, K. K., Cantrell, W., Chang, K., Ciochetto, D., Niedermeier, D., Ovchinnikov, M., Shaw, R. A., and Yang, F.: Aerosol indirect effect from turbulence-induced broadening of cloud-droplet size distributions, Proc. Natl. Acad. Sci. U. S. A., 113, 14243–14248, https://doi.org/10.1073/pnas.1612686113, 2016.

Chandrakar, K. K., Morrison, H., and Witte, M.: Evolution of Droplet Size Distributions During the Transition of an Ultraclean Stratocumulus Cloud System to Open Cell Structure: An LES Investigation Using Lagrangian Microphysics, Geophys. Res. Lett., 49, 1–10, https://doi.org/10.1029/2022GL100511, 2022.

Dziekan, P., Jensen, J. B., Grabowski, W. W., and Pawlowska, H.: Impact of Giant Sea Salt Aerosol Particles on Precipitation in Marine Cumuli and Stratocumuli: Lagrangian Cloud Model Simulations, J. Atmos. Sci., 78, 4127–4142, https://doi.org/10.1175/JAS-D-21-0041.1, 2021.

Grabowski, W. W.: Comparison of Eulerian bin and Lagrangian particle-based schemes in simulations of PI chamber dynamics and microphysics, J. Atmos. Sci., 77, 1151–1165, https://doi.org/10.1175/JAS-D-19-0216.1, 2020.

Grabowski, W. W., Andrejczuk, M., and Wang, L. P.: Droplet growth in a bin warm-rain scheme with Twomey CCN activation, Atmos. Res., 99, 290–301, https://doi.org/10.1016/j.atmosres.2010.10.020, 2011.

Grabowski, W. W., Kim, Y., and Yum, S. S.: CCN Activation and Droplet Growth in Pi Chamber Simulations with Lagrangian Particle–Based Microphysics, J. Atmos. Sci., 81, 1201–1212, https://doi.org/10.1175/jas-d-24-0004.1, 2024.

Grabowski, W. W., Morrison, H., Shima, S. I., Abade, G. C., Dziekan, P., and Pawlowska, H.: Modeling of cloud microphysics: Can we do better?, Bull. Am. Meteorol. Soc., 100, 655–672, https://doi.org/10.1175/BAMS-D-18-0005.1, 2019.

Grabowski, W. W. and Pawlowska, H.: Technical note: Phase space depiction of cloud condensation nuclei activation and cloud droplet diffusional growth, Atmos. Chem. Phys., 25, 5273–5285, https://doi.org/10.5194/acp-25-5273-2025, 2025.

Hansen, J. E., Kharecha, P., Sato, M., Tselioudis, G., Kelly, J., Bauer, S. E., Ruedy, R., Jeong, E., Jin, Q., Rignot, E., Velicogna, I., Schoeberl, M. R., von Schuckmann, K., Amponsem, J., Cao, J., Keskinen, A., Li, J., and Pokela, A.: Global Warming Has Accelerated: Are the United Nations and the Public Well-Informed?, Environ. Sci. Policy Sustain. Dev., 67, 6–44, https://doi.org/10.1080/00139157.2025.2434494, 2025.

Hoffmann, F. and Feingold, G.: Cloud microphysical implications for marine cloud brightening: The importance of the seeded particle size distribution, J. Atmos. Sci., 78, 3247–3262, https://doi.org/10.1175/JAS-D-21-0077.1, 2021.

Intergovernmental Panel on Climate Change (IPCC): Climate Change 2021 – The Physical Science Basis, Climate Change 2021 – The Physical Science Basis, Cambridge, United Kingdom, https://doi.org/10.1017/9781009157896, 2021.

Morrison, H., Chandrakar, K. K., Shima, S.-I., Dziekan, P., and Grabowski, W. W.: Impacts of Stochastic Coalescence Variability on Warm Rain Initiation Using Lagrangian Microphysics in Box and Large-Eddy Simulations, J. Atmos. Sci., 81, 1067–1093, https://doi.org/10.1175/jas-d-23-0132.1, 2024.

Park, M., Yum, S. S., Seo, P., Ahn, C., Kim, N., Anderson, B. E., and Thornhill, K. L.: A New CCN Number Concentration Prediction Method Based on Multiple Linear Regression and Non-Negative Matrix Factorization: 2. Application to Obtain CCN Spectra in and Around the Korean Peninsula, J. Geophys. Res. Atmos., 128, https://doi.org/10.1029/2023JD039234, 2023.

Park, M., Yum, S. S., Seo, P., Kim, N., and Ahn, C.: A New CCN Number Concentration Prediction Method Based on Multiple Linear Regression and Non-Negative Matrix Factorization: 1. Development, Validation, and Comparison Using the Measurement Data Over the Korean Peninsula, J. Geophys. Res. Atmos., 128, https://doi.org/10.1029/2023JD039189, 2023.

Prabhakaran, P., Thomas, S., Cantrell, W., Shaw, R. A., and Yang, F.: Sources of Stochasticity in the Growth of Cloud Droplets: Supersaturation Fluctuations versus Turbulent Transport, J. Atmos. Sci., 79, 3145–3162, https://doi.org/10.1175/JAS-D-22-0051.1, 2022.

Seinfeld, J. H., Bretherton, C., Carslaw, K. S., Coe, H., DeMott, P. J., Dunlea, E. J., Feingold, G., Ghan, S., Guenther, A. B., Kahn, R., Kraucunas, I., Kreidenweis, S. M., Molina, M. J., Nenes, A., Penner, J. E., Prather, K. A., Ramanathan, V., Ramaswamy, V., Rasch, P. J., Ravishankara, A. R., Rosenfeld, D., Stephens, G., and Wood, R.: Improving our fundamental understanding of the role of aerosol-cloud interactions in the climate system, Proc. Natl. Acad. Sci. U. S. A., 113, 5781–5790, https://doi.org/10.1073/pnas.1514043113, 2016.

Shaw, R. A., Thomas, S., Prabhakaran, P., Cantrell, W., Ovchinnikov, M., and Yang, F.: Fast and slow microphysics regimes in a minimalist model of cloudy Rayleigh-Bénard convection, Phys. Rev. Res., 5, 1–14, https://doi.org/10.1103/PhysRevResearch.5.043018, 2023.

Shima, S., Kusano, K., Kawano, A., Sugiyama, T., and Kawahara, S.: The super-droplet method for the numerical simulation of clouds and precipitation: A particle-based and probabilistic microphysics model coupled with a non-hydrostatic model, Q. J. R. Meteorol. Soc., 135, 1307–1320, https://doi.org/10.1002/qj.441, 2009.

Thomas, S., Ovchinnikov, M., Yang, F., van der Voort, D., Cantrell, W., Krueger, S. K., and Shaw, R. A.: Scaling of an Atmospheric Model to Simulate Turbulence and Cloud Microphysics in the Pi Chamber, J. Adv. Model. Earth Syst., 11, 1981–1994, https://doi.org/10.1029/2019MS001670, 2019.

Thomas, S., Prabhakaran, P., Yang, F., Cantrell, W. H., and Shaw, R. A.: Dimensionless parameters for cloudy Rayleigh-Bénard convection: Supersaturation, Damköhler, and Nusselt numbers, Phys. Rev. Fluids, 7, 1–15, https://doi.org/10.1103/PhysRevFluids.7.010503, 2022.

Thomas, S., Yang, F., Ovchinnikov, M., Cantrell, W., and Shaw, R. A.: Scaling of Turbulence and Microphysics in a Convection–Cloud Chamber of Varying Height, J. Adv. Model. Earth Syst., 15, https://doi.org/10.1029/2022MS003304, 2023.

Wang, A., Ovchinnikov, M., Yang, F., Cantrell, W., Yeom, J., and Shaw, R. A.: The Dual Nature of Entrainment-Mixing Signatures Revealed through Large-Eddy Simulations of a Convection-Cloud Chamber, J. Atmos. Sci., 81, 2017–2039, https://doi.org/10.1175/JAS-D-24-0043.1, 2024.

Yang, F., Hoffmann, F., Shaw, R. A., Ovchinnikov, M., and Vogelmann, A. M.: An Intercomparison of Large-Eddy Simulations of a Convection Cloud Chamber Using Haze-Capable Bin and Lagrangian Cloud Microphysics Schemes, J. Adv. Model. Earth Syst., 15, 1–20, https://doi.org/10.1029/2022MS003270, 2023.

Yang, F., Sadi, H. F., Shaw, R. A., Hoffmann, F., Hou, P., Wang, A., and Ovchinnikov, M.: Microphysics regimes due to haze–cloud interactions: cloud oscillation and cloud collapse, Atmos. Chem. Phys., 25, 3785–3806, https://doi.org/10.5194/acp-25-3785-2025, 2025.